ACOUSTIC ENERGY HARVESTING USING DUAL PIEZOELECTRIC PLATES

by

Maleka AbdulBari Bin Tarsh

A Thesis presented to the Faculty of the
American University of Sharjah
College of Engineering
In Partial Fulfillment
of the Requirements
for the Degree of

Master of Science in
Mechatronics Engineering

Sharjah, United Arab Emirates

May 2017

Approval Signatures

We, the undersigned, approve the Master's Thesis of Maleka AbdulBari Bin Tarsh.

Thesis Title: Acoustic Energy Harvesting using Dual Piezoelectric Plates.

Signature	**Date of Signature** (dd/mm/yyyy)
_____	_____
Dr. Jin-Hyuk Lee Assistant Professor, Department of Mechanical Engineering Thesis Advisor	
_____	_____
Dr. Maen Alkhader Assistant Professor, Department of Mechanical Engineering Thesis Committee Member	
_____	_____
Dr. Lutfi Albasha Associate Professor, Department of Electrical Engineering Thesis Committee Member	
_____	_____
Dr. Lotfi Romdhane Director, Mechatronics Engineering Program	
_____	_____
Dr. Mohamed El-Tarhuni Associate Dean for Graduate Affairs and Research College of Engineering	
_____	_____
Dr. Richard Schoephoerster Dean, College of Engineering	
_____	_____
Dr. Khaled Assaleh Interim Vice Provost for Research and Graduate Studies	

Acknowledgements

First of all, this research would not have been completed without the blessings of Almighty Allah for granting me this opportunity to do my masters at AUS. I would like to thank my family for their love and support through my entire life.

I want to express my sincere gratitude to my advisor Dr. Jin-Hyuk Lee for his constant supervision, guidance, support, and motivation throughout my research stages. I'm deeply thankful for his invaluable input, advice and knowledge.

I also would like to thank the Mechatronics department for providing me with equipped laboratory to run my experiments. Also, especial thanks to Eng. Kent Roferos for his great assistance during my experiments.

I also want to extend my sincere appreciation to the staff at the manufacturing laboratory for providing me with the necessary equipment and for their massive help.

Also, I want to thank my friends for their support and good times. This thesis would not have been possible without them.

To my family

Abstract

Sound is abundant energy found in our everyday lives, especially in urban places. Acoustic energy can be thought of as a good alternative energy source. Despite the fact that the sound is prevalent; it is challenging to scavenge energy for practical application due to the low-power density. However, the harvested energy from acoustics can be used to power low-power electronic devices. Researchers have established various techniques and mechanisms to increase the harvested energy at the low frequency range. One widely famous and effective mechanism is the use of piezoelectric (PZT) transducers. This technique has been used by many researchers to maximize the energy harvested from sound (vibration). Dual piezoelectric cantilever plates will be employed to harness the acoustic waves and obtain the natural frequency. The natural frequency is first determined through a proposed mathematical model and it is found to be 247 Hz. Then, the natural frequency is verified by a numerical method used by COMSOL Multiphysics software and it is found to be 242 Hz. This frequency is then validated with experimental data and it found to be 239 Hz; which is close to the mathematical and simulation results. The dual piezoelectric cantilever plates will be placed inside a quarter-wavelength straight-tube resonator. The tube resonator works as an amplifier when an incident wave travels through it. An acoustic resonant wave is applied and drives the PZT plates causing it to generate energy. The amplification ratio is 3.58 dB at the resonant frequency (239 Hz). Several tests are carried out to validate the resonant frequency within the tube resonator and it is verified to be 239 Hz. Furthermore, multiple tests are conducted with tube resonator placed at different locations from the acoustic source. Those tests confirmed that the maximum voltage is produced at the resonant frequency (239 Hz). The goal of this research is to find an improved way to harvest the currently wasted acoustic/vibration energy through piezoelectric cantilever plates.

Keywords: ***Piezoelectric; PZT; energy harvesting; natural frequency; low frequency; Cantilever; FEM; COMSOL***

Table of Contents

List of Figures

List of Tables

Chapter 1: Introduction

1.1. Introduction

Energy harvesting has been a topic of an interest to most of the researchers [1-10], where they have developed ways to convert the ambient energy in the environment into electrical energy. The term energy harvesting is used for low-scale power generation in which the power generated is in the scale of micro-to-milli-watts. Harvesting energy from thermal [4], solar [11], wind [12], mechanical vibration [13], has been investigated theoretically and experimentally for powering low-power devices. However, acoustic energy compared with other energy sources has received the least attention to develop harvesting methods. The acoustic energy is abundant, free, sustainable and clean energy source that can be extracted and converted into electrical energy.

The acoustic waves convey energy that causes some element to vibrate and possibly to deform a structure thereby generating electricity. Recently, there have been significant efforts to develop mechanism to harvest the acoustic energy from airports, road traffic, construction sites, and work plants [9]. Moreover, the conversion of mechanical vibration (sound) to electricity can be done using three types of generators, namely, electromagnetic, electrostatic, and piezoelectric generators. Amongst the three mechanisms, piezoelectric transduction has received the greatest attention.

Piezoelectric (PZT) is a smart alternative for batteries, which can create energy on the go. Many researches were conducted around this topic. The first micromachined acoustic energy harvester was introduced by Horowitz *et al.* as it used Helmholtz resonator with piezoelectric ring attached to one of the walls [1]. He was able to achieve maximum power of ~0.1 nW at frequency of 13.6 kHz. Then on the same concept, Liu *et al.* [2] developed an electromechanical Helmholtz resonator that utilizes the uniform pressure of the incident wave in the resonator chamber to bend the piezoelectric plate. This work generated power of 30 mW at 2.6 kHz frequency, this power is enough to supply low powered electronic devices. Kim *et al.* [4] used the Helmholtz resonator to harvest airflow and aeroacoustic energy using the magnet driven by acoustic pressure principle and they were able to generate 4 mV voltage at 1.4 kHz frequency. Lallart *et al.* [5] tried to improve the power gain in acoustic energy harvesting at a high frequency. Most of the above studies generated power/voltage at high frequencies which can be

found in military and governmental communication systems, aviation, and over the horizon radar system. However, these applications are not used on daily basis. Therefore, the need to harvest acoustic energy from low frequencies that are found in our daily life such as TVs, traffic, sirens at 30m, jet engines and many other sound sources, is examined and studied in this work. Nevertheless, all the previous studies generated power using single piezoelectric beam and dual piezoelectric beams configuration has not been investigated. Therefore, the main objective of this research is to develop a new method to harvest energy from low frequency sound waves using dual piezoelectric beams. This approach is able to double the harvested energy since dual PZTs are employed. To attain the maximum output power density from the PZT, the PZTs' frequency should match the excitation frequency. The resonant frequency is confirmed mathematically and through simulation in COMSOL software to optimize the dimensions of the PZT plates. And then various experiments are executed to validate the resonant frequency of the PZT system with the specific boundary condition (BC). After, designing an appropriate PZT setup, a quarter-wavelength tube resonator will be fabricated to amplify the voltage generated from the PZT setup.

1.2. Literature Review

Li, and You [6], utilized the Helmholtz resonator to maximize the energy harvested from piezoelectric plates. They managed to change shape of the Helmholtz resonator to have rectangular shape to increase the sound pressure amplification factor. Also, the rectangular shape of the tube will minimize the eigenfrequency and bring it down to be around 400 Hz. In this study, two tests were conducted; one with single beam and the second is with nine beams placed inside the tube resonator. The single beam showed energy storage of 0.0569 μJ when the sound pressure level applied is 100 dB. The number of beams was increased to be 9 beams and the output energy was 0.382 μJ. Though, the total stored energy of the 9 beams is greater than that of the single beam that does not mean the total energy increases linearly with the increase of the beam number inside the tube. This is due to the interaction of the air particles with the beams. Therefore, a limited number of beams must be placed inside the tube that will ensure high energy output. Moreover, the energy generated cannot be used to power devices.

Therefore further studies on different energy sources that show high voltage generation is investigated. An extraction of renewable energy from rain drops and wind speeds were investigated by Vatansever *et al.* [7]. The voltage was generated from these

natural phenomena using ceramic based piezoelectric fiber composite structures (PFCs) and polymer based piezoelectric strips, PVDF (Polyvinylidene fluoride), to be used in powering small devices. After running various experiments on both piezoelectric materials and changing the parameters such as the wind speed, the weight of droplets and the releasing height, conclusions were drawn. The greater the height and the larger the mass of the water drops, the higher voltage was generated. The energy scavenging depends on the geometric dimension of the material and the type of films. Finally, it was proven that the peak voltage was higher, relative to the ceramic piezoelectric materials, when the polymer based piezoelectric material was used in this application. From there on further studies on piezoelectric material is conducted and their application. Based on [7], Li *et al.* [8] use PZT beams based piezoelectric material in tube resonator. Two different in length tube resonators were designed to test the output voltage of the piezoelectric material plates. A 52 cm and 42 cm tube resonator study the effect of using the two piezoelectric materials that are PVDF and PZT respectively. For the 52 cm tube resonator it showed a voltage generation of 0.105 V and 55.6 nW when single PVDF beam was placed near the open inlet. On the other hand, the 42 cm tube generated voltage and power density of 1.433 V and 0.193 mW, respectively, when single beam was placed. Then, the voltage and power were increased when 5 to 7 beams of PVDF were placed in the 52 cm tube and the output voltage and power are 0.42V and 171.48 nW at 100 dB. However, the PZT in the 42 cm tube showed 9 and 1813 times higher voltage and power increase than the PVDF, when 4 to 6 beams were placed (3.789 V and 0.311 mW, respectively). Then, they harvested travelling sound of a low frequency inside a 42 cm straight tube resonator that is open from one end and contains lead zirconate titanate (PZT) cantilever plates. The working mechanism is that when the incident travelling sound frequency matches the resonator resonance frequency the amplified acoustic pressure inside the tube excites the vibration motion of the piezoelectric plates, causing voltage generation. The amplification factor for the first eigenfrequency (199 Hz) was 97.2. The voltage generated at 100 dB with 4 PZT plates, is 5.089 V and when the incident sound pressure was increased to 110 dB, the voltage produced increased to 15.689 V, in which it was concluded that there is a linear relationship between the voltage and the incident sound pressure. The corresponding power is 12.697 mW and the areal (power per unit area) and volume power densities are 0.635 mW cm^{-2} and 15.115 µW cm^{-3}, respectively [9]. Then, building on the same result of [14], they were able to simulate the quarter-wave length resonator using

commercial finite element software (COMSOL software). The amplification factor for the simulated model was 100.1 at the first eigenfrequency (198 Hz) and the amplification factor for the experimental model was 97.2 at 199 Hz. When a single PZT was simulated at 100 dB, it generated 1.6 V at 196 Hz. When it was compared to the experimental data, it was close as it generated 1.43 V at 199 Hz. Then, the number of PZT plates was increased to 4 PZT, generating 0.37 mW at 190 Hz. Subsequently, beams were increased to 5 PZT plates and it generated 4.06 V at 189 Hz. It can be concluded that the experimental data are 7% and 19% lower than the simulation results (3.79 V at 193 Hz and 0.31 mW at 194 Hz) [10]. Then Li *et al.* [6], tested the 58 cm tube resonator with PVDF cantilever beams and placed them in two configurations aligned and zigzag. The zigzag configuration showed significant increase in the voltage and power relative to the aligned configuration. The zigzag configuration has more open path for the acoustic air particle motion, which leads to higher amplification ratio. The first three eigenfrequencies that are 146 Hz, 439 Hz, and 734 Hz the amplification ratios are 59.1, 42.2, and 23.3, respectively. The maximum voltage when multiple PVDF beams were used is 0.696 and the power is 0.31 μW at 100 dB. And due to the linear relationship between the sound pressure level (SPL) and the output voltage, the voltage was increased to 1.48 V when the pressure level reached 110 dB [8].

1.3. Thesis Methodology

The previous studies have focused on harvesting energy through a tube resonator [6, 7, 9, 10, 14], where multiple piezoelectric beams were used in specific configuration. The multiple beams were placed successively from the open inlet towards the closed inlet of the tube resonator to harvest energy. The output voltage decreases as the piezoelectric beams move to the close inlet. Moreover, the number of piezoelectric beams that can be placed and hence the output voltages are limited because of the interaction of the acoustic air particles inside the resonator.

In order to solve this problem, two piezoelectric cantilevers are placed vertically on top of each other near the open end inlet of the quarter-wavelength tube resonator. This method is anticipated to double the voltage scavenged when the resonant frequency of the PZT matches the exciting frequency. A mathematical model is developed to calculate the resonant frequency of the PZT. Then, numerical simulations are performed using COMSOL software, to verify the resonant frequency. The resonant frequency of the system is compared against the mathematical and simulation models,

through experimental procedure. After that, a quarter-wavelength tube resonator is designed, fabricated and tested to amplify the output voltage of the system.

1.4. Research Contribution

A novel PZT configuration is suggested in this research to harvest acoustic energy from the surrounding environment. This configuration amplifies the energy harvested with fewer PZTs at low frequency. A new mathematical model is proposed to model the PZT plates. The PZT plate model is simulated to validate the mathematical model and compare it against it. The mathematical model is then validated against the finite element (FE) simulation. Based on the results of the designed PZT system a customized tube resonator is built to amplify the harvested energy.

1.5. Thesis Organization

This thesis starts with the introduction including background information about energy harvesting followed by literature review about the previous methods to harness energy from acoustics. The preliminary studies on piezoelectric and the design of both the cantilever PZTs as well as the tube resonator are presented in Chapter 2. Chapter 3 models the cantilever PZT through nonconventional mathematical method. Through the mathematical model, the natural frequencies of the system are obtained and to study the behavior of the system when it is directed to a harmonic force. The cantilever PZT design setup is numerically simulated using the finite element analysis software COMSOL and it is documented in Chapter 4. Also, in Chapter 4, the analytical model is confirmed using experimental data and the small discrepancy is explained. The simulation of the tube resonator is presented in Chapter 5. Furthermore Chapter 5 contains the experimental apparatus and the results of the tube resonator. Finally, Chapter 6 concludes and summarizes the findings and proposes ideas for future research.

Chapter 2: Literature Survey

In this chapter, an early investigation about vibration-based energy harvesting using the piezoelectric transduction is done. A summary about the basic transduction techniques to convert vibration to electricity is discussed. Also, the advantages of selecting the piezoelectric transduction amongst other mechanisms are investigated. Based on the piezoelectric transduction selection, the theory of the piezoelectric effect is presented. Further studies on the cantilever configuration, choice of material, and the suitable harvester design configuration are discussed. Then, the analytical relationship between the output voltage and the displacement of the piezoelectric when a mechanical stress, is examined. Finally, a brief description about the practical application of the piezoelectric is presented.

2.1. Vibration-Based Harvesting Mechanism

Over the last decade energy harvesting has gained special attention especially vibration-based energy. Researchers have developed many methods to harvest vibrational energy and convert it into electricity for microsystems [15]. This unexploited mechanical energy (vibration) can be harvested through three basic mechanisms that are electromagnetic [16, 17], electrostatic [18, 19], and piezoelectric [20, 21] transductions. The electromagnetic transducer is widely used in low frequency ranges for medium size devices. The electromagnetic transducer has high compatibility level with Si microsystems technology [22]. It also operates in higher frequency range (50 Hz); in which generates higher power density [23]. However, the high cost of integrating it with a microsystem is one of the drawbacks since it is complex to design and manufacture. Another disadvantage is the bulky size of the permanent magnets and the timing coil. The second mechanism is the electrostatic, which is the best fit mechanism for MEMS applications and it does not need smart material. But this type requires external voltage source such as battery to charge and has mechanical constraints. The last transducer is piezoelectric transducer which is commonly used. This is due to the property of the material that makes it very attractive, where these materials have large power density, compact configuration, high coupling in sole crystal and high feasibility for daily applications [24]. Piezoelectricity is the property where electricity is generated from mechanical stress. It is form of charges stored in the solid materials like ceramics, crystals, and bones when a pressure is applied. This property

of piezoelectric materials makes them attractive in energy scavenging. The piezoelectric material can withstand huge amount of strain magnitude to convert mechanical energy into electrical energy compared to other transductions. Figure 1 represents the high power density of the piezoelectric compared with other mechanism verses voltage.

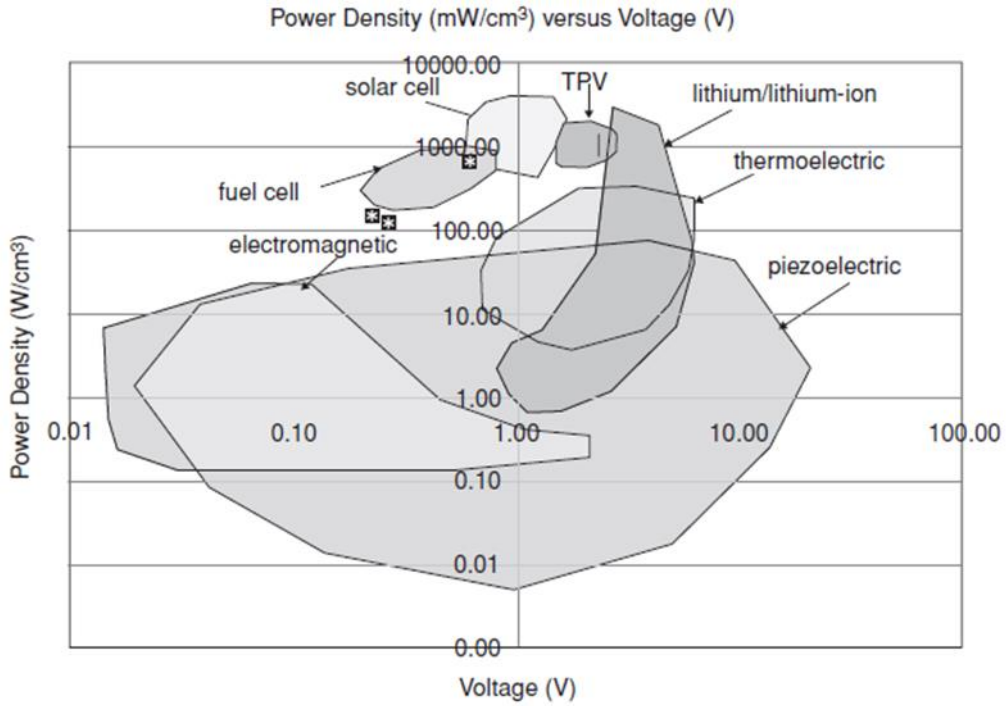

Figure 1: Power density vs. voltage [14]

2.2. Theory

In 1880, Pierre and Jacques Curie discovered the piezoelectric effect. Piezoelectricity is the linear relation between the electric potential and mechanical stress in a crystal. When mechanical stress is applied in crystal or solid materials, an electric field is generated. This property of piezoelectric materials makes them attractive in energy scavenging.

There are two forms of piezoelectric effect that are the direct and the converse effect. The direct effect is the change of electric polarization when strain is applied. In other words, when mechanical stress (tensile or compressive) is applied due to external force, it will alter the separation between the positive and the negative charges in the crystal leading to net polarization at the surface. The effect of the piezoelectric has proportional relation with the symmetry of the material. The more symmetric the crystal is the more electric polarization produced. Then, in 1881, Gabriel Lippmann found out

that piezoelectric materials exhibit the reverse piezoelectric effect. In a similar manner, the converse effect (reciprocal) is whereby a piezoelectric crystal changes when the electric field is applied, causing the material to produce mechanical strain [25]. As an example of application that uses converse effect is the motors and ultra-exact, while the microbalances and scanning microscopy are examples that employ the direct piezoelectric. In addition, the direct piezoelectric effect is accountable for the material's ability to act as a sensor and the converse piezoelectric effect is accountable for its ability to act as an actuator [26].

There are coupled linear mathematical equations that describes the piezoelectric effect and they are as follows:

$$\boldsymbol{S} = \boldsymbol{s^E}.\boldsymbol{T} + \boldsymbol{d^t}.\boldsymbol{E} \quad (1)$$

$$\boldsymbol{D} = \boldsymbol{d}.\boldsymbol{T} + \boldsymbol{\varepsilon^T}.\boldsymbol{E} \quad (2)$$

where S is the mechanical strain vector, T is the mechanical stress vector, D is the electric displacement (charge density), E is the electric field, s^E is the compliance (strain produced by unit stress), ε^T is the dielectric permittivity, while d and d^t are the matrices for the direct and converse piezoelectric effect (the *t* indicates transpose). Both equations can be extended to describe 6 mm crystal class such as PZT ceramic [27].

2.3. Piezoelectric Actuators

Piezoelectric actuators consist of two main categories that are: stack actuators and stripe actuators (bending actuators). The stack actuators consist of layers of piezoelectric mounted vertically on top of each other. They have low stroke, high blocking force and the total volume increases the output energy. The stripe actuators are multi-layers of piezoceramics that are fixed either as double or single ended i.e. cantilever [28]. The stripe actuator has large stroke and very limited blocking force relative to the stack actuator. A special type of stripe actuator is the piezoelectric bimorph actuator.

A stripe bending actuator with triple layers from APC International, Ltd. is used as displayed in Figure 2. The stripe actuator is designed to create a fairly large mechanical deflection when an electrical voltage is applied. One layer of the piezoelectric bimorph expands and the other contracts [29]. Figure 2, shows a bimorph PZT piezoelectric consist of two thin strips of piezoelectric sandwiching a carbon fiber

layer as central shim. The two piezoelectric (piezoceramic) layers are bonded together in a way that the direction of polarization is matching. Also, these stripes are connected electrically together in parallel manner in which this configuration ensures high sensitivity for any input. This design of actuator achieves relatively higher deflection compared to other designs and configurations. According to [30], the maximum deflection can reach up to 2.5 mm for a cantilever mounting structure for any regular magnitude actuator.

The stripe actuator is modelled as multi-layer cantilever beam. A beam is a long, slender structure that is capable of withstanding transverse loading which results in bending effects (as seen in Figure 2).

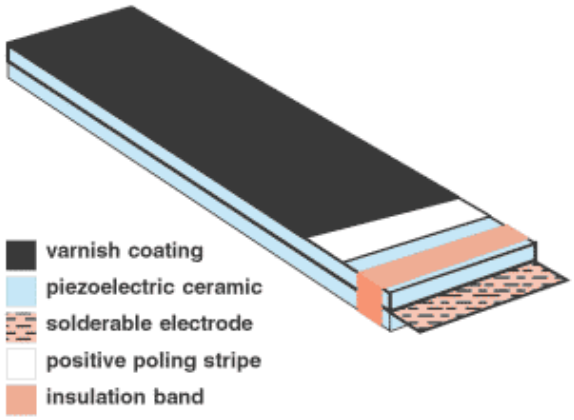

Figure 2: Bimorph PZT configuration [30]

The PZT three parallel layers consist of two piezoceramic layers and one carbon fiber layer in the middle. The carbon fiber layer is longer by 5.5mm than the other two layers. The piezoceramic layers are coated with electrical insulation to protect it from the environmental changes like dust, humidity and other hazards. Also, there are two solderable electrodes, positive and negative, to connect the PZT with any electrical connection [30].

2.4. Cantilever Configuration

The geometry of the PZT affects the amount of energy harvested especially mechanical energy harvesting from vibration. Typically cantilever shaped PZT is mostly used in vibration-based energy harvesting. Cantilever configuration has one edge clamped and the other edge is moving freely. Most of the resonance frequency of the cantilever is lower than the other vibration modes of the piezoelectric element.

Consequently, the design of cantilever devices involves a unimorph or a bimorph cantilever beam/plate. Moreover, the construction of cantilever beam is simple and easier to get low resonant frequency (~100 Hz). Cantilever structure is preferred over two edge-clamped bridge structure because it can generate larger mechanical strain when a same input force is applied, similarly when cantilever structure is compared to all-edge-diaphragm.

In cantilever structure, the strain is at its maximum at the clamped edge and it starts to decrease when moving further away from the clamped part. Therefore, the non-stressed portion does not contribute to the total power generated [31]. It was therefore chosen as the configuration to this thesis.

2.5. Choice of Material

Piezoelectric ceramic materials are used in energy harvesting devices due to their properties, low cost, and the ease to be combined into energy harvesting devices. Among all of the piezoelectric ceramics, the Lead Zirconate Titanate (PZT) is attractive material for energy harvesting because of the high Curie temperature and its excellent properties. Over the past decades [32], the PZT has expanded and modified using chemical composition and fabrication processes to include broad range of piezoelectric properties. Some of the frequently used piezoelectric include PZT-5H, PZT-5A, and PZT-5X. Piezoelectric ceramics can be used based on the mechanical energy source. As an example when harvesting energy from vibration, thin and thick films of ceramic piezoelectric, and plates are preferred because they can be easily integrated with the cantilever. But if the energy is to be harvested from mechanical impacts, layers of piezoelectric ceramic can be used to increase the efficiency since the bimorph has more efficiency than the monomorph due to its polarity.

Roundy *et al.* [31] developed an energy harvesting device using bimorph PZT bimorph cantilevers. It harvested energy from low level vibration to power wireless sensor nodes. First, Roundy was able to build PZT cantilever using PZT-5A ceramic piezoelectric and steel center shim to reduce the resonance frequency of the cantilever. A proof mass was attached to the end of the cantilever too. The device was driven a vibration at 100 Hz which matches the natural frequency of the PZT. The output power recorded was 60 µW. Then, he was able to enhance the device by using two cantilevers using PZT-5H, and it was able to produce about 200 µW and 380 µW.

Sodano *et al*., in 2003, stated that when dimension of 63.5x60.3x0.27 mm^3 of PZT-5H cantilever is driven on an electromagnetic shaker at the resonance frequency (50 Hz), the cantilever was able to charge a 1000 mAh NiMH rechargeable battery to 90% of the battery's capacity within 22 hours [33].

In this study, a PZT-5X piezoelectric bimorph cantilever is used to convert the sound wave from the loudspeaker into electricity. This is due to its large deflection, force lead or no lead, competitive price and availability.

2.6. Piezoelectric Harvester Design Configurations

The main objective of this work is to employ piezoelectric material in energy harvesting application. Consequently, the focus is on the independent elements in the coupling *d* tensor. In *d* tensor, there are three elements; d_{15}, d_{31} and d_{33}. The d_{15} is related to shear stress, while d_{31} and d_{33} are related to energy harvesting. Therefore, the later *d* tensor elements will be described in details. The 31 mode is where the vibration force is applied perpendicular to the poling direction. The second mode 33, is where the applied force on the same side as the poling direction. The first number (3) indicates that the voltage is generated in the z axis. The second number specifies the direction in which the stress is applied. In 33 operation mode, the stress and voltage are of the same direction. While in the 31 mode, the stress is applied along the x axis and the voltage appears in the z axis. The 31 mode is commonly used for energy harvesting applications. Many energy harvesting structures, like cantilevers and double clamped beam, work in the 31 mode. This is because the lateral stress on the surface of the beam is easily coupled to the deposited material on the beam. Therefore, the d_{31} mode is of our interest in this study. Thus for the 31 mode, the stress equation can be re-written as follows [31]:

$$\boldsymbol{S_{11} = s_{11}^{E}.T_1 + d_{31}.E_3} \tag{3}$$

2.7. Relationship between PZT plate deflection and Voltage

After realizing the relation between the electric and mechanical vectors, a more specific study between the deflection of the PZT and the voltage generated is analyzed. The bimorph piezoelectric actuator has similar working principle as that of the thermostatic bimetals. When the ceramic is energized, it creates a bending moment and the substrate that is coupled with the piezoelectric actuator deflects. The deflection motion is proportional to the applied voltage. Also, the bending moment transforms the

small change in length into large bending displacement vertical to the contraction. Displacements of millimeters can be completed within microseconds. Therefore, an estimation of the bending displacement of the three layers connected in parallel is calculated [34] as follows:

$$\Delta L_{bend} = \frac{3}{8} * n * d_{31} * \frac{l_f^2}{h_p^2} \frac{1 + R_h}{1 + 1.5R_h + 0.75R_h^2 + 0.125R_E R_h^3} V \qquad (4)$$

Table 1 shows all the parameter of the bending actuator equation and their respective numerical values.

Table 1: Piezoelectric bender equation parameter

Symbols	Representation	Values	Units
n	number of stacked layers	3	-
d_{31}	deformation coefficient	750p	m/V
l_f	free length of PZT	0.03	m
h_p	height of the piezoceramic	0.0007	M
R_h	ratio of substrate height (h_s) and piezoceramic element height (h_p)	$\boldsymbol{R_h} = \frac{h_s}{h_p} = \frac{0.00022}{0.00048} = 0.4583$	-
R_E	ratio of the moduli of elasticity of substrate (E_s) and piezoceramic element (E_p)	$\boldsymbol{R_E} = \frac{E_s}{E_p} = \frac{2GPa}{40GPa} = 0.05$	-
V	Operating voltage	2.20	V

The bending displacement depends on many parameters that are: the number of ceramic layers, the deformation coefficient, the free length of the actuator, the height

of the actuator and the operating voltage. The operating voltage depends on the thickness of a single layer of the actuator. After defining the parameters of the bending displacement of the multi-layer bending actuator, it is then substituted in Eq. 4. The bending displacement is $5.27x10^{-9}m$ when voltage of 1V is applied.

2.8. Applications of Piezoelectric

The piezoelectric effect was not utilized well in the first period after its discovery and practical application were limited. Pierre and Jacques described piezoelectric devices for static measurement of various parameters. Due to the properties of the piezoelectric it is possible to transform electricity into acoustical signals and vice versa. The property of the piezoelectric crystal allows it to produce accurate quantity of electric charge. This property works well in the construction of precision devices' [35]. An illustration of piezoelectric effect and its applications is displayed in Figure 3.

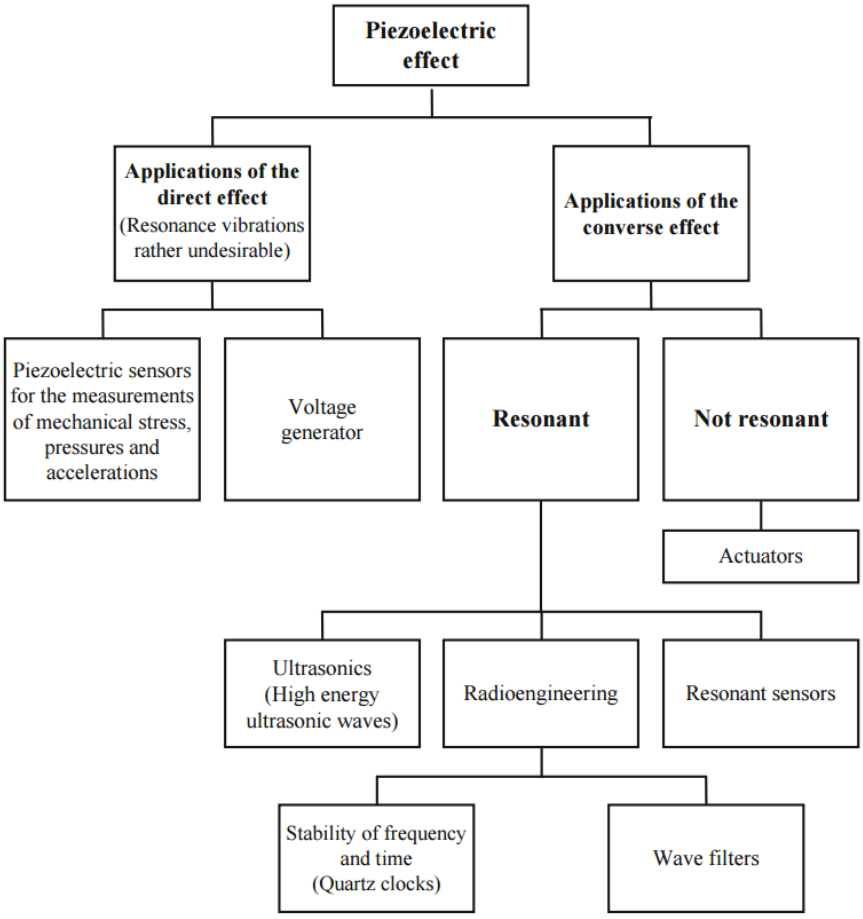

Figure 3: Piezoelectric application [35]

2.9. Tube Resonator

Acoustic resonators are known for their absorption application, sound augmentation [36] and noise attenuation [37]. Acoustic resonator such as tube resonator works as energy storage. When an incident sound wave excites the tube resonator resonant frequency, acoustic energy is produced inside it. This energy comes in resonating standing wave shape. There are three types of acoustic resonators namely Helmholtz resonator (HR), half-wavelength and quarter-wavelength resonator as seen in Figure 4.

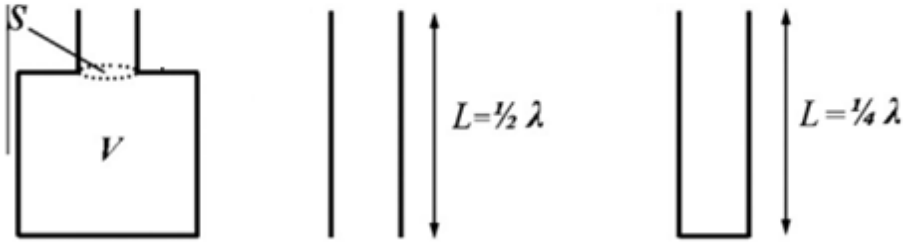

Figure 4: Schematic of the resonators: from left to right: a) Helmholtz, b) Half-wavelength, c) Quarter-wavelength resonators [2]

2.9.1. Helmholtz Resonator (HR)

A Helmholtz resonator is shaped as neck and cavity. The resonator is represented as spring, mass damper as seen in Figure 5. It operates when an incident sound wave frequency matches the resonators eigenfrequency. When the air in the HR neck vibrates, it acts like a mass and the air in the cavity acts like spring since it expands and experiences compression too. The energy dissipation happens when there is a friction between the wall and the air [14].

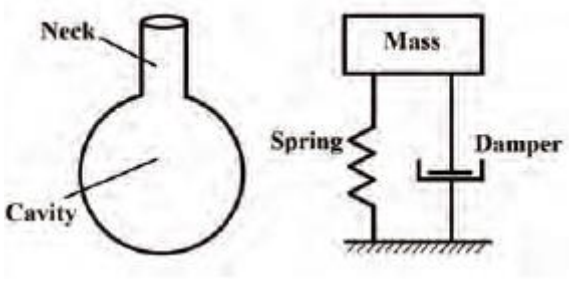

Figure 5: Helmholtz resonator [10]

2.9.2. Half-wavelength Resonator

As seen from Figure 4b, the half-wave resonator is a straight tube that is open from both ends. Since the tube is open from two ends, there is not enough pressure.

Therefore, each end must be an antinode, a point of maximum vibration, for the air motion. The center of the tube is a node for the vital mode and where the pressure is high. Half-wavelength resonator is of a great deal in industrial application such as combustion chamber [38].

2.9.3. Quarter-wavelength Resonator

A quarter-wavelength tube resonator is a tube with one end open and the second is closed unlike the half-wave resonator. The quarter-wavelength tube cannot be modelled as lumped parameter like the HR. A study between the half wavelength and quarter-wavelength is conducted to analyze the efficiency of accumulating acoustic energy. It was experimentally proven that quarter-wavelength stores three times more energy than half-wavelength at the same input frequency [39]. In further experiment, the quarter wavelength resonator was proven to harvest more energy than Helmholtz resonator at the same volume and frequency [39].

In this work, a suitable resonator that is efficient in the acoustic energy harvesting field must be chosen. Since both the HR and half-wavelength are used in the industrial applications like combustion chamber. Thus, the quarter wavelength resonator falls within these criteria and hence it is selected.

The travelling waves in the quarter-wavelength tube are determined by the boundary condition at the ends of the tube. The boundary conditions are dependent on acoustic pressure, longitudinal particle velocity or impendence. In the closed end of the tube, the velocity is zero and the pressure is zero. For the open end, the velocity and the pressure are at maximum. The pressure $P_n(z)$ and the longitudinal particle velocity $u_n(z)$ are related in sinusoidal function as [9]:

$$P_n(z) = P_{0n} \sin \frac{\pi(2n-1)z}{2L} \tag{5}$$

$$u_n(z) = u_{0n} \cos \frac{\pi(2n-1)z}{2L} \tag{6}$$

where z is the distance from the open inlet along the tube

The corresponding resonance frequency is expressed as:

$$f = \frac{(2n-1)c_0}{4L} \tag{7}$$

where c_0 is the speed of the sound in the air, n is an integer mode number and L is the length of the tube. As one can see from Eq. 7 the resonant frequency is function of the length of the tube. Therefore, changing the length of the tube can change the resonance frequency. Moreover, since the first resonance frequency is of our interest then (n=1).

Chapter 3: Mathematical Model

A mathematical model for the bimorph PZT plates is established to calculate the natural frequency and analyze the vibrational effect. The mathematical model is derived based on the Galerkin method, which is used to determine the stiffness and mass matrices of the beam. The Bernoulli-Euler beam theory is also introduced to investigate the PZT plate. The PZT plates are considered as composite cantilever beam and thus its parameters are designed. Furthermore, the Galerkin method provides a solution for the modal analysis where the natural frequencies are evaluated.

3.1. Literature Review

Various mathematical models have been established to analyze the behavior of the smart structure when piezoelectric sensors and actuator are incorporated within them. There are two main groups when analyzing the smart structures that are: induced strain models and coupled electromechanical models. The induced strain models neglect the electric potential, while the electromechanical models include the electrical potential and the displacement. The induced strain models predict the actuator behavior of the piezoelectric materials. Chee *et al.* [40] formulated an analytical composite smart structure with higher order displacement. The model was developed using the Hamilton's variational principle and validated using finite element analysis. Another study by Beheshti-Aval and Lezgy-Nazargah [41] modeled a laminated structure using the coupled electromechanical model. The composite beam is bonded with piezoelectric actuators and sensors where sinus model is employed to model the mechanical displacement. The layer theory is applied on each piezoelectric layer to study the variation of the electric potential and model it. This led to developing a two-nodded Hermitian layer-wise nodded part for beam with multiple layers. The model is valid for different loading types whether mechanical or electrical. In similar approach a finite element modeling of the plate with known location of the piezoelectric sensors and actuators embedded in a plate is presented in [42]. Hamilton's principle is utilized to find the finite element equations through ANSYS software. Then the analytical solutions are compared to the numerical solution developed using Kirchhoff's plate theory. Then the static and dynamic analysis of the symmetric patches of the piezoelectric bonded in the plate are investigated in 2D. In another related work [43], a finite element analysis of structure with piezoelectric sensors and actuator is developed

in one dimensional (1D) plane. This method uses Euler-Bernoulli method and presumes a bilinear distribution of the electric potential across the beam. The analyses were conducted on steel beam along with studying the sensitivity. Then using modal analysis, the three first eigenfrequencies were evaluated and provided good results. Similar study is done by Reddy *et al.* [44] where he develops a higher order theory for laminated composite plates. This theory considers the transverse shear strains throughout the thickness of the plates. An exact solution of the symmetric layers is obtained and compared with first order shear deformation theory. The higher order theory is better than the first order theory in terms of calculating the deflections and stresses.

Previous studies have modeled the smart structures with piezoelectric sensors and actuators lumped to it as a plate and solved it accordingly [41, 43, 44]. They also used the coupled electromechanical model to predict the sensors and the actuator behavior of the piezoelectric. However, in this thesis, the piezoelectric beam itself will be modeled as cantilever beam rather than embedding it within structure. The cantilever beam will be clamped at one end thus it is more likely to be modeled as beam element than a plate element since we are only interested in the deflection motion not the other two rotation motions of the plate [45]. Moreover the piezoelectric is treated as a sensor hence it is efficient to model it to work as sensor only. Therefore, it is more suitable to model the PZT beam as 2 DOF composite beam element using the elementary beam theory.

3.2. Beam Theory

Theories related to beams theory take huge part in analyzing several structures in solids. The beam theory is a simple tool for designers to analyze the beam models and other structures. Although there are more advanced tools like finite element analysis, yet the beam theory is a basic tool for any designer. The calculations in beam theory provide insight into the structure and fundamental computational solutions. Many beam theories are developed and each offers diverse number of solutions and levels of accuracy. One of the simplest and commonly used theory is the Euler Bernoulli theory. The Euler Bernoulli theory covers the bending characteristics of a beam [46].

The bending effect was discovered by researchers and was recognized as an important factor in transversely vibrating beam. The bending effect relationship with the elasticity of the curvature of the beam was discovered by Jacob Euler (1654-1705). Then his nephew, Daniel Bernoulli (1700-1782), formulated the differential equations

for vibrating beam. Then in 1707, Bernoulli's theory was accepted by Leonhard Euler while discovering the shape of the elastic beam under different loading circumstances. After, Euler's many trials and a development on the elastic curves of the beam, the beam theory was established. It is a simple and good engineering approximation for many problems [47]. The Euler Bernoulli beam theory assumes an infinite rigidity of the cross section of the beam in its plane that there exists no defamation in this section. Therefore, the in-plane displacements of the cross section represented as two rigid body translational and one rigid body rotation [46].

3.3. Mathematical Formulation

The stripe PZT actuator mentioned in section 2.3 is modeled as single composite cantilever beam. The cantilever beam has two degrees of freedom (DOF) that is transverse deflection and rotation. The deflection occurs when the beam is exposed to a force or bending moments at its tip node. In our case, the PZT is subjected to harmonic sound wave causing it to deflect around its local axial coordinate at the free end (unclamped end).

Figure 6, shows the three layers of the cantilever beam PZT. The carbon layer in the middle is longer than the other layers by 0.005 m and for simplicity it is considered to have the same length as the other layers (0.035 m). The PZT is clamped at the longer part of the carbon fiber layer and is free to vibrate at the other end. This helps the mathematical model derivation with ease.

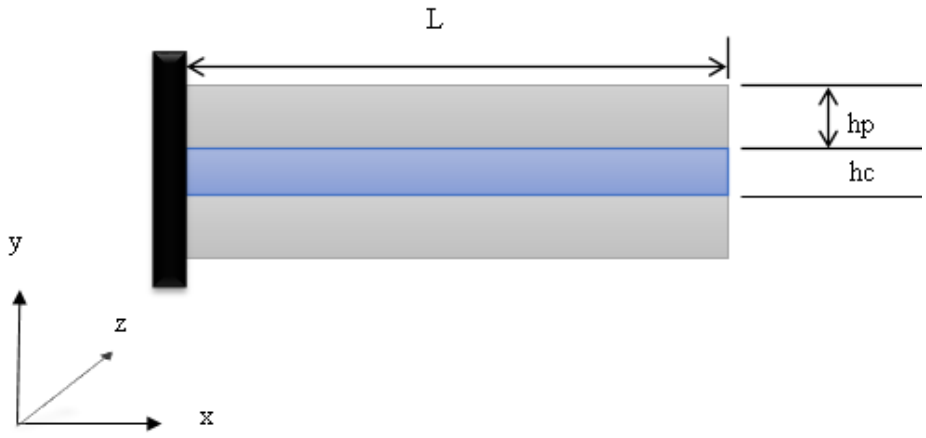

Figure 6: Multilayer cantilever beam

The governing differential equation of the piezoelectric cantilever beam in 2D will be analyzed in section 3.3.1.

3.3.1. Equation of motion of beam element

The equation of motion for a linear-elastic beam can be described by the following differential equation. Figure 7, shows the acting shear forces (*V*) and bending moments (*M*) on a beam element.

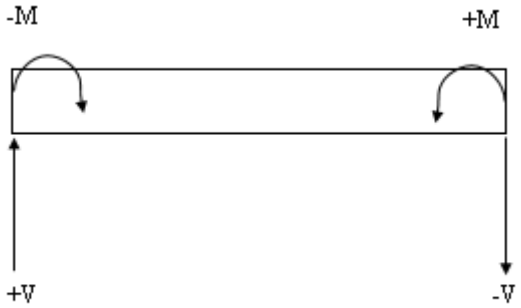

Figure 7: Shear forces and bending moments on beam

The shear forces, the bending moments and the loading force *w(x)* of the beam at equilibrium is calculated as:

$$\sum F_y = 0 \tag{7}$$

$$V - (V + dV) - w(x)dx = \rho A(x)dx\frac{\partial v}{\partial t} \tag{8}$$

Where *V* is the shear force, ρ is the mass density, *A(x)* is the cross sectional area of the beam and $\hat{v}$ is the transverse displacement function in the $\hat{y}$ direction.

The moment equation about the y axis leads to:

$$\sum M_2 = 0 \tag{9}$$

$$-(V + dV)dx + dM + w(\hat{x})dx(\frac{dx}{2}) = 0 \tag{10}$$

Then, by arranging $dV = \frac{\partial V}{\partial x}$ and $dM = \frac{\partial M}{\partial x}dx$

when dividing the equation by ∂x and taking the limit of the equation as $d\hat{x}$ approaches 0, then $w(\hat{x})$ will disappear.

Then the following equation will relate the shear force (*V*) with the bending moment (*M*):

$$V = \frac{\partial M}{\partial x} \tag{11}$$

From the above equations

$$-\frac{\partial^2 M}{\partial x^2} + w(\hat{x}) = \rho A(x) dx \frac{\partial^2 V}{\partial t^2} \tag{12}$$

Moreover, the moment of the beam is related to the curvature *k* of the beam as follows:

$$k = \frac{M}{EI} \tag{13}$$

where *E* is the elastic modulus and *I* is the moment of inertia about the *z* axis. The moment of inertia for rectangular cross section is given by:

$$I = \frac{bh^3}{12} \tag{14}$$

where *b* is the base (width) and *h* is the height

The curvature for small slope ∅ is given by:

$$k = \frac{\partial \widehat{\emptyset}}{\partial y} = \frac{\partial^2 v}{\partial x^2} \tag{15}$$

A relation can be found between the transverse displacement and the shear force to obtain differential equation:

$$\frac{\partial^2 v}{\partial x^2} = \frac{M}{EI} \tag{16}$$

Inserting Eqs. 13 and 14, we obtain the equation of the motion for the forced transverse vibration:

$$\frac{\partial^2}{\partial x^2}\left(EI\frac{\partial^2 v}{\partial x^2}\right) + \rho A \frac{d^2 v}{dt^2} = w(\hat{x}) \tag{17}$$

For free vibration force$w(x) = 0$, thus it becomes:

$$\frac{\partial^2}{\partial x^2}\left(EI\frac{\partial^2 v}{\partial x^2}\right)+\rho A\frac{d^2 v}{dt^2}=0 \tag{18}$$

The equation of motion for the linear-elastic beam is given by the following differential equation:

$$EI\frac{d^4 v}{dx^4}+\rho A\frac{d^2 v}{dt^2}=0 \tag{19}$$

where the beam equation includes the mass and stiffness terms and neglects the damping term. The stiffness matrix and the consistent-mass matrix (CMM) will be developed as well as the equations for a beam element and then it will demonstrate a complete system of equation for the beam [48].

3.3.2. Boundary Condition

The boundary conditions must be specified otherwise the stiffness matrix [K] will be singular. In other words, the determinant of the stiffness matrix will be zero which leads to unstable system. Specifying boundary conditions will prevent the system from moving as rigid body and will allow it to resist different applied loads. In this case, the boundary condition that makes [K] non-singular is two, where the number of boundary condition depends on the number of nodal displacement. The boundary conditions for the system are applied at nodes 1 and 2 as shown in Figure 8:

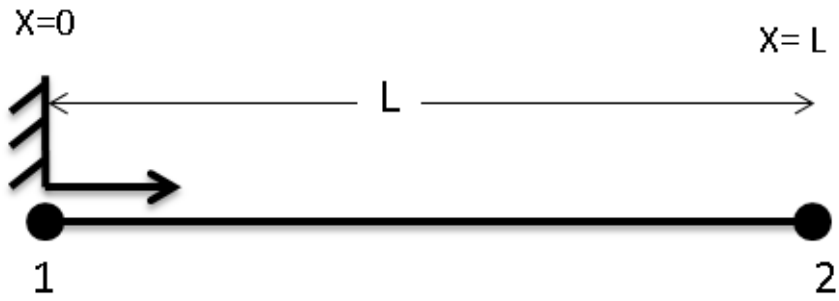

Figure 8: Boundary condition for beam element

The boundary conditions are:

$$\left[EI(\frac{d^4 v}{dx^4})\delta(\frac{d^4 v}{dx^4})\right]_0^L=0 \tag{20}$$

$$\left[\frac{\partial}{\partial x}(EI(\frac{d^4v}{dx^4})\delta v\right]_0^L = 0 \tag{21}$$

where $m = EI\left(\frac{d^4v}{dx^4}\right)$ is the bending moment, δ is the displacement, and $\frac{\partial}{\partial x}(EI(\frac{d^4v}{dx^4})$ is the shear force. The analysis of these equations will be done through the finite element method. In which the solution is assumed in the form of polynomial and it is substituted in the equation of motion of the beam. Therefore, the assumed solution will have residue left out and all the equations will not be satisfied. Thus the Galerkin method will be used to reduce the residue and have better results.

3.3.3. Galerkin Method

There are various methods to find the stiffness matrix for a beam which are the direct method, variational method, and the Galerkin method. The first method is more suitable for computer-automated analysis of complex structures. The second method involves the calculation of the potential energy of the structure and the load in order to minimize the error term [49]. However, the last method is useful for developing the element equations. This method is used when information about the energy of the system is unknown like the potential energy, kinetic energy. The methods of residuals applied directly to the differential equation can be used to develop the finite element equations. There are many residual methods like the least squares and least squares collocation. However, the Galerkin method is chosen in calculating the stiffness matrix in the finite element method and in implementation.

At first, the solution will be assumed as a polynomial describing the transverse displacement variation through the element length to be:

$$u(x,t) = a + bx + cx^2 + dx^3 \tag{22}$$

In which it is a polynomial of 3rd order because there are 4 degrees of freedom (DOF), the motions are transverse displacement u_i and small rotation at each node φ_i. Also, the cubic function satisfies the basic beam differential equation and the conditions of displacement. Moreover, the cubic function fulfills the boundary conditions of the displacement. The cubic polynomial equation can be described in matrix form as:

$$u(x,t) = [N_1 \quad N_2 \quad N_3 \quad N_4] \begin{Bmatrix} u_1 \\ u_2 \\ u_3 \\ u_4 \end{Bmatrix} \tag{23}$$

$$u(x,t) = [N(x)]\{u(t)\} \tag{23.a}$$

Where

$$N_1 = 1 - 3\frac{x^2}{L^2} + 2\frac{x^3}{L^3}$$

$$N_2 = x - 2\frac{x^2}{L^2} + \frac{x^3}{L^2}$$

$$N_3 = 3\frac{x^2}{L^2} - 2\frac{x^3}{L^3}$$

$$N_4 = -\frac{x^2}{L} + \frac{x^3}{L^2}$$

N_1, N_2, N_3, N_4 are shape functions for a beam element and they are functions of *x*, while *u* is function of *t*. When the beam element is evaluated at node 1, $N_1 = 1$ and at node 2 $N_1 = 0$. And $N_3 = 0$ at node 1, and at node 2, $N_3 = 1$. Shape functions N_2 and N_4 their derivatives have similar properties.

Therefore, when the solution is substituted in the equation of motion the residue will be:

$$R = \frac{\partial^2}{\partial x^2}\left(EI\frac{\partial^2 v}{\partial x^2} + \rho A\frac{d^2 v}{dt^2}\right) \tag{24}$$

Now to reduce the residue it will be multiplied by shape function and be equated to zero:

$$\int_0^L R * N_i \, dx = 0 \qquad i = 1,2,3,4 \tag{25}$$

$$\int_0^L N_i(x)(EI\frac{d^4 v}{dx^4} + \rho A\frac{d^2 v}{dt^2})dx = 0 \tag{26}$$

Then to have complete solution, the elastic part will be integrated using integration by parts to yield to:

$$= N_i \frac{d}{dx}\left(EI_{yy}\frac{d^2v}{dx^2}\right) - N_i'\left(EI_{yy}\frac{d^2v}{dx^2}\right) + \int N_i'' EI_{yy}\frac{d^2v}{dx^2}\, dx \tag{27}$$

The displacement equation will be substituted in the equation of motion to get the elemental matrix:

$$= \int_0^L [N_i]^{-1}\, \rho A \frac{d^2v}{dt^2} dx + \int_0^L [N''_i]^{-1} EI_{yy}\frac{d^2v}{dx^2}\, dx \tag{28}$$

where *i=1,2,3,4* since there are four shape functions.

Therefore the expanded elemental matrix is:

$$= \begin{Bmatrix} [N_1\ (EI_{yy}u''(x,t))']_0^L \\ [N_2\ (EI_{yy}u''(x,t))']_0^L \\ [N_3\ (EI_{yy}u''(x,t))']_0^L \\ [N_4\ (EI_{yy}u''(x,t))']_0^L \end{Bmatrix} + \begin{Bmatrix} [N'_1\ EIu''(x,t)]_0^L \\ [N'_2\ EIu''(x,t)]_0^L \\ [N'_3\ EIu''(x,t)]_0^L \\ [N'_4\ EIu''(x,t)]_0^L \end{Bmatrix} \tag{29}$$

Simplifying and substituting the displacement yields to:

$$= \int_0^L \rho A [N_i]^{-1}[N_i]\, dx\, [\ddot{u}(t)]^{-1} + \int_0^L EI_{yy}[N'']^{-1}[N'']\, dx [\ddot{u}(t)]^{-1} \tag{30}$$

The first part represents the mass matrix [M], while the elastic second term represents the stiffness matrix. The stiffness matrix can be found from the integration by substituting the shape functions and since *u(t)* is function of *t*, it could be left out of the integration:

$$[K] = \int_0^L EI_{yy}[N'']^{-1}[N'']\, dx \tag{31}$$

$$[K] = \int_0^L EI_{yy} \begin{Bmatrix} N_1'' \\ N_2'' \\ N_3'' \\ N_4'' \end{Bmatrix} [N_1'' \quad N_2'' \quad N_3'' \quad N_4'']\, dx \tag{31.a}$$

$$[K] = \int_0^L EI_{yy} \begin{pmatrix} N_1''N_1'' & N_1''N_2'' & N_1''N_3'' & N_1''N_4'' \\ \vdots & \ddots & : & \vdots \\ N_4''N_1'' & \cdots & \ldots & N_4''N_4'' \end{pmatrix} \tag{31.b}$$

when integrating:

$$[K_{beam}] = \frac{EI_{yy}}{L^3}\begin{bmatrix} 12 & 6L & -12 & 6L \\ 6L & 4L^2 & -6L & 2L^2 \\ -12 & -6L & 12 & -6L \\ 6L & 2L^2 & -6L & 4L^2 \end{bmatrix} \quad (32)$$

It is noted that the elements of the stiffness matrix are symmetric and that is statement of Maxwell's Reciprocity Theorem:

$$K_{ij} = K_{ji}$$

The stiffness matrix relates the nodal displacement {d} to the forces {F} at the nodes as:

$$\{F\} = [K]\{d\} \quad (33)$$

In a similar manner, the consistent-mass matrix can be evaluated,

$$[M] = \int_0^L \rho A[N_i]^{-1}[N_i]\, dx \quad (34)$$

$$[M] = \int_0^L \rho A \begin{bmatrix} N_1^2 & \cdots & N_{14} \\ \vdots & \ddots & \vdots \\ N_{41} & \cdots & N_4^2 \end{bmatrix} dx \quad (34.a)$$

$$[M_{beam}] = \frac{\rho AL}{420}\begin{bmatrix} 156 & 22L & 54 & -13L \\ 22L & 4L^2 & 13L & -3L^2 \\ 54 & 13L & 156 & -22L \\ -13L & -3L^2 & -22L & 4L^2 \end{bmatrix} \quad (34)$$

3.3.4. Equivalent beam parameters

The PZT beam consists of two different isotropic materials with different parameters such as the Young's modulus, mass density and thickness. In order to obtain the mathematical model for the bi-material beam element, the stiffness and mass matrices must consider the mixture of the piezoceramic and carbon fiber. The parameters of the new composite beam element will be evaluated. The composite consists of 3 layers with top and bottom piezoceramic and carbon fiber in the center. The piezoceramic layers are symmetric and the mixture can therefore be reduced to 2 different layers i.e. pizeoceramic and carbon fiber making the parameters of our PZT easier to compute.

The procedure of the calculating the composite beam element parameters can be divided into two parts that is calculating the parameters of the consistent-mass matrix

and stiffness matrix. First step is calculation of the total mass density for the two materials. Afterward the beam element is scaled to find the equivalent moment of inertia and subsequently the area. Next step is to obtain the equivalent Young's modulus and to evaluate the effective length of the beam. After calculating these variables, they will be used to calculate the equivalent mass and stiffness matrices and perform modal analysis.

Firstly, the mass of components of the composite beam is calculated. The mass density is defined as the mass over volume. The mass density of a mixture of two materials (piezoceramic and carbon fiber) is added with respect to the volume. Figure 9, shows the three layers that can be transformed into one mass by adding the mass of each layer.

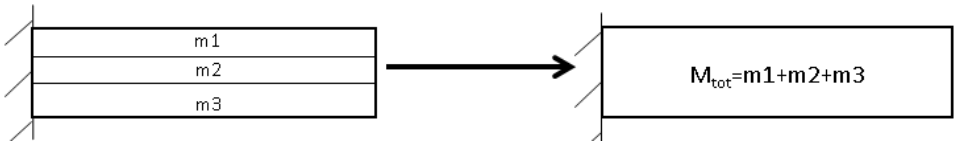

Figure 9: Equivalent mass density

Since the volume of each of the materials is additive hence the mass density for each layer is added. The following addition applies:

$$\rho_{tot} V_{tot} = \rho_p V_p + \rho_c V_c \tag{35}$$

where $\rho_{tot}$is the total mass density of the beam is, V_{tot} is the total volume of the beam, ρ_p is the mass density of piezoceramic, V_p is the volume of the piezoceramic, while $\rho_c$is the mass density of the carbon fiber and V_c is the volume of the carbon fiber.

Substituting for the volume:

$$\rho_{tot}(h_{tot} * b * L) = \rho_p(h_p * b * L) + \rho_c(h_c * b * L) \tag{36}$$

where, h_{tot} is the total height of the beam, b is the width of the beam, h_p is the height of the piezoceramic layer, and h_c is the height of the carbon fiber layer.

$$\rho_{tot} h_{tot} = \rho_p h_p + \rho_c h_c \tag{37}$$

The total mass density of the beam is then obtained as follows:

$$\rho_{tot} = \rho_p \frac{h_p}{h_{tot}} + \rho_c \frac{h_c}{h_{tot}} \tag{38}$$

After calculating the total mass density, the stiffness of the material is analyzed through scaling the composite beam by evaluating an equivalent area. The equivalent area represents the stiffness of the second material i.e. carbon fiber which has low stiffness. In other words, the size of the equivalent piezoceramic layer differs by the ratio of the Young's modulus of both materials as given in Eq. 39. Since the carbon fiber has lower Young's modulus than the pizeoceramic layer thus more material is needed to maintain the same strain distribution and the same load as the original shape. Figure 10b, shows the scaled area of the composite beam element.

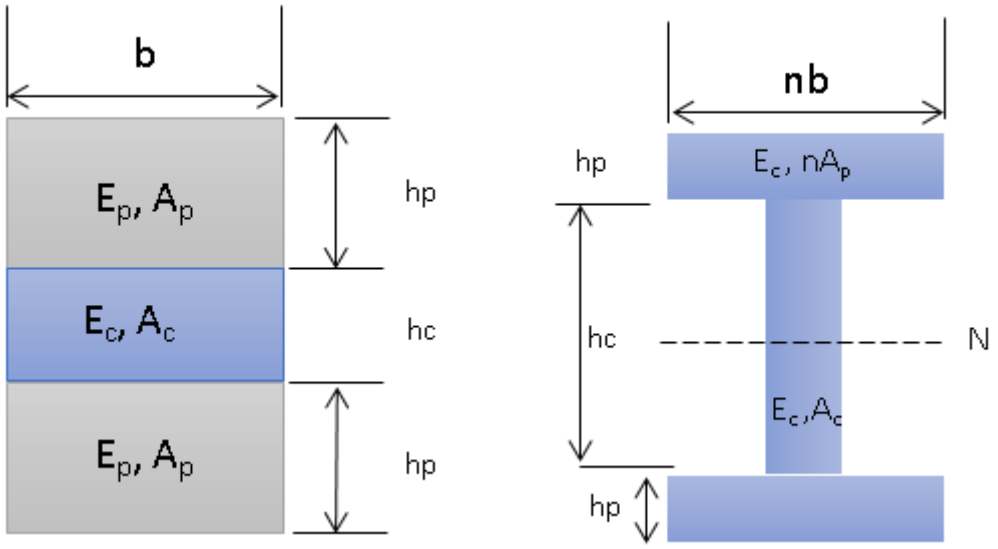

Figure 10: a) Cross section of the beam b) equivalent cross section of the beam

The area is scaled in the horizontal direction because the dimensional change should be perpendicular to the loading plane. In this case the loading plane is vertical to the beam. Therefore, to account for the stiffness difference the area is scaled to the carbon fiber material through *n*.

$$n = \frac{E_p}{E_c} \tag{39}$$

where *n* is the ratio of the Young's modulus for the carbon fiber E_c and the Young's modulus of the piezoceramic E_p

Then the new moment of inertia is calculated at the centroid of the full transformed area around the neutral axis as represented in Figure 11. And the new width of the transformed material is found as:

$$w = n * b \tag{40}$$

where *w* is the new width of the beam, *b* is the width of original beam element

Using the new width, the moment of inertia can be calculated for the transformed section as follows:

$$I = \frac{b_c {h_c}^3}{12} + 2(\frac{w {h_p}^3}{12} + Ad^2) \tag{41}$$

Where

$$A = w * h_p \tag{42}$$

And *d* is the distance from the center of the upper or lower layer to the centroid as shown in Figure 11.

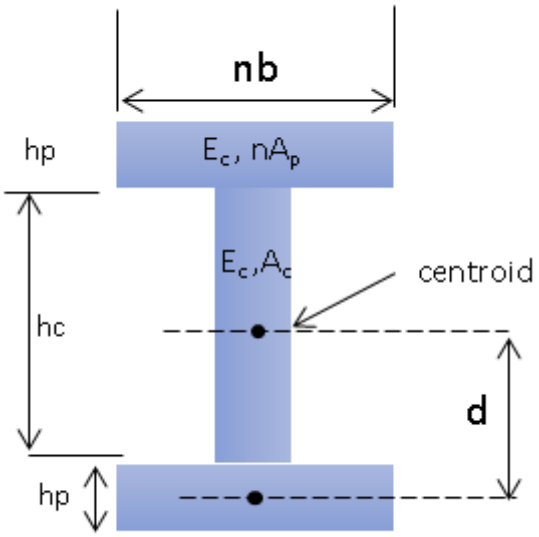

Figure 11: Equivalent cross section

Since the transformed beam element consists of one material that is carbon fiber hence the total Young's modulus is the carbon fiber Young's modulus. Finally, it should be noted that the length of the carbon fiber layer is longer than the piezoceramic layer by 5.5 mm. Therefore, the beam is clamped at the edge of the carbon fiber layer so the

effective carbon layer length is the same as the piezoceramic length. The calculated parameters are tabulated in Table 2:

Table 2: Parameters of the beam element

Parameters	Value	Unit (SI)
Mass density (ρ)	5.36×10^{3}	Kg/m^3
Moment of Inertia (I)	11.096×10^{-12}	m^4
Area (A)	1.42×10^{-5}	m^2
Young's modulus (E)	2G	Pa
Length (L)	0.035	m

3.4. Frequency Response Analysis

After assembling the element matrix and evaluating the global matrices for the mass and stiffness, the global system of equation can be obtained. In frequency response analysis, the structural dynamic of a system is calculated at the excitation frequency. This analysis solves coupled matrix equation through complex algebra. The forced vibration equation of the PZT bending actuator with harmonic excitation is given by:

$$[M]\{\boldsymbol{\ddot{x}(t)}\} + [C]\{\boldsymbol{\dot{x}(t)}\} + [K]\{\boldsymbol{x(t)}\} = \{\boldsymbol{F(w)}\} \tag{43}$$

where M is the mass matrix, C is the damping coefficient matrix, K is the stiffness matrix, F is the forcing sinusoidal force of angular frequency w, and x is the transverse displacement

In the undamped free vibration case, the damping factor and the force will be cancelled (C=0) and (F=0). Therefore, the homogenous equation is written as:

$$[M]\{\boldsymbol{\ddot{x}(t)}\} + [K]\{\boldsymbol{x(t)}\} = \mathbf{0} \tag{44}$$

The solution for the complex harmonic motion is assumed as:

$$\{X\} = \{\boldsymbol{u(w)}\}e^{jwt} \tag{45}$$

$$\{\dot{X}\} = jw\{\boldsymbol{u(w)}\}e^{jwt} \tag{46}$$

$$\{\ddot{X}\} = (jw)^2\{\boldsymbol{u(w)}\}e^{jwt} = -w^2\{\boldsymbol{u(w)}\}e^{jwt} \tag{47}$$

where u is a constant vector, which will be determined later.

Substituting the solution into the differential equation:

$$(-[M]w^2 + [K])\{\boldsymbol{u}(\boldsymbol{w})\}e^{jwt} = \mathbf{0} \tag{48}$$

where $e^{jwt} \neq 0$

Therefore,

$$(-[M]w^2 + [K])\{\boldsymbol{u}(\boldsymbol{w})\} = \mathbf{0} \tag{49}$$

where *M* is the global consistent-mass matrix, *w* is the natural frequency, *K* is the global stiffness matrix.

The natural frequency can be acquired through finding the determinant consisting of the mass and stiffness matrices:

$$\det\left(-w^2[M_g] + [K_g]\right) = 0 \tag{50}$$

Therefore, the numerical values of the global consistent-mass and stiffness matrices were computed in MATLAB to acquire the angular frequency (*w)*. There are 4 possible combinations of the natural frequency. But only the first 2 natural frequencies are calculated. The natural frequency is computed as follows:

$$f = \frac{w}{2\pi} \tag{51}$$

The system natural frequency can be compared with the theoretical natural frequency and the numerical FEM method in the next chapter.

The mode (eigenvector$\{\boldsymbol{u}(\boldsymbol{w})\}$) of each the frequencies (eigenvalue *w*) is determined by solving the differential equation after acquiring the natural frequency. The eigenvectors are the mode shapes of the system. The mode shape of the system is calculated as:

$$(-[M]w^2 + [K])\{\boldsymbol{u}(\boldsymbol{w})\} = 0 \tag{52}$$

$$[K]\{\boldsymbol{u}(\boldsymbol{w})\} = w^2[M]\{\boldsymbol{u}(\boldsymbol{w})\} \tag{53}$$

Let

$$\boldsymbol{X} = \{\boldsymbol{u}(\boldsymbol{w})\} \tag{54}$$

And

$$\lambda = w^2 \tag{55}$$

Thus, the equation that holds the generalized eigenvalues and eigenvector is:

$$K\boldsymbol{X} = \lambda M\boldsymbol{X} \tag{56}$$

The eigenvalues are obtained through MATLAB and they are

$$f_1 = 247Hz \text{ and} f_2 = 1545Hz.$$

Figure 12 shows the cantilever beam at the first mode. The resonant frequency at the first mode is 247 Hz. The first mode shows the displacement of the beam from the fixed end at t=0.

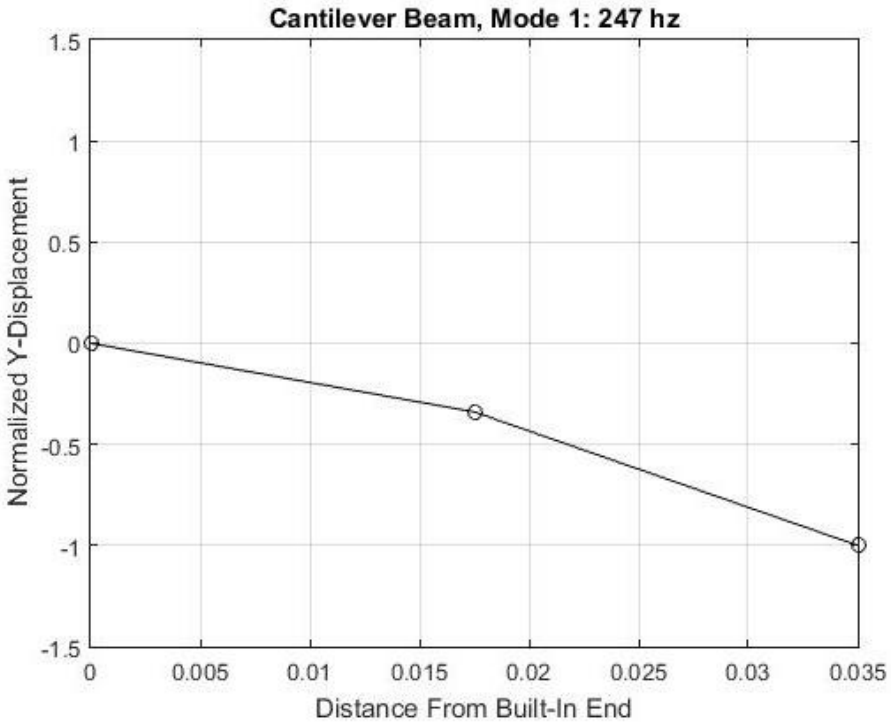

Figure 12: The first mode at f = 247 Hz

Figure 13 shows the second mode of the beam. The second natural frequency is found to be 1558 Hz. In this mode, the beam oscillates around the deflection axis. In this case, a minimum of two elements is chosen to be able to view the second mode. As time progress the second mode and higher modes will oscillate around the zero displacement.

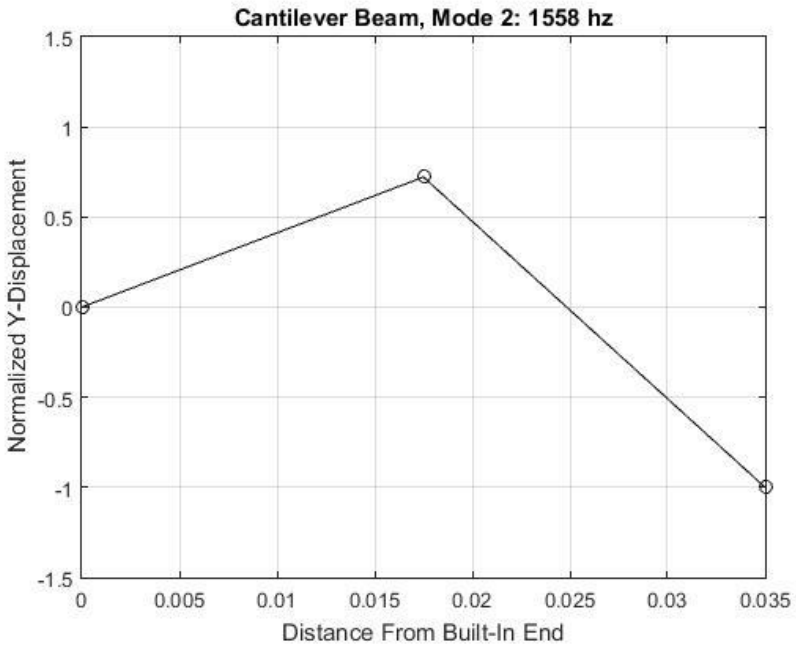

Figure 13: The second mode at 1545 Hz

Figure 14, shows the resonant frequency for all the modes of the beam when 2 elements are selected.

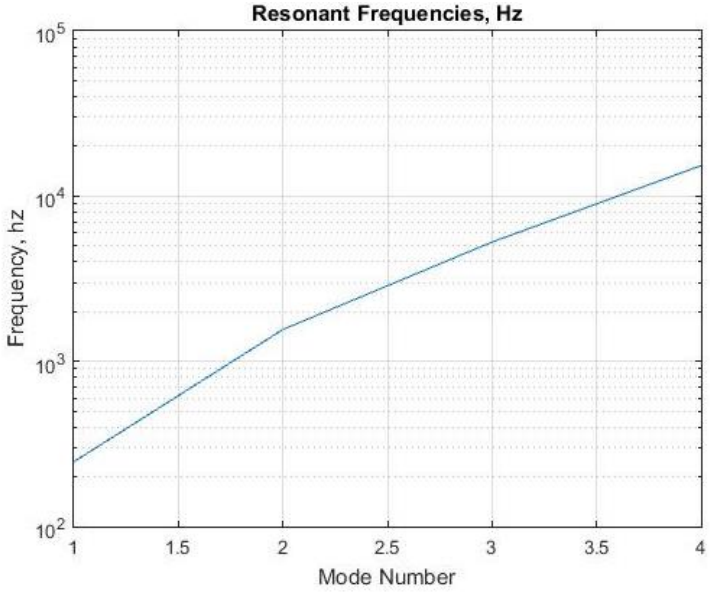

Figure 14: Resonant frequencies verses the mode shapes

Then, a harmonic force representing the acoustic wave from the subwoofer is applied to the beam to analyze the amplitude of the resonant frequency. The differential equation of the complex harmonic motion is now solved for the nonhomogeneous part that is when a plane wave is applied at the beam:

$$[\boldsymbol{M}]\{\boldsymbol{x}(\ddot{\boldsymbol{t}})\} + [\boldsymbol{K}]\{\boldsymbol{x}(\boldsymbol{t})\} = [\boldsymbol{F}] \tag{57}$$

where

$$F = \begin{Bmatrix} f_1 \\ f_2 \\ f_3 \\ f_4 \end{Bmatrix} \tag{58}$$

And since only the force applied at the tip of the beam is of our interest then the force vector is re-written as:

$$F = \begin{Bmatrix} f_1 \\ 0 \\ 0 \\ 0 \end{Bmatrix} \tag{59}$$

where

$$f_1 = A\sin(wt + \theta) \tag{60}$$

where A is the maximum amplitude of the sine wave (A=1), w is the angular frequency and Θ is phase shift.

Figure 15, shows the resonant frequency and the corresponding amplitude of the first two modes when the force is applied at the tip. From Figure 15, it shows that the first natural frequency at 247 Hz has the highest amplitude.

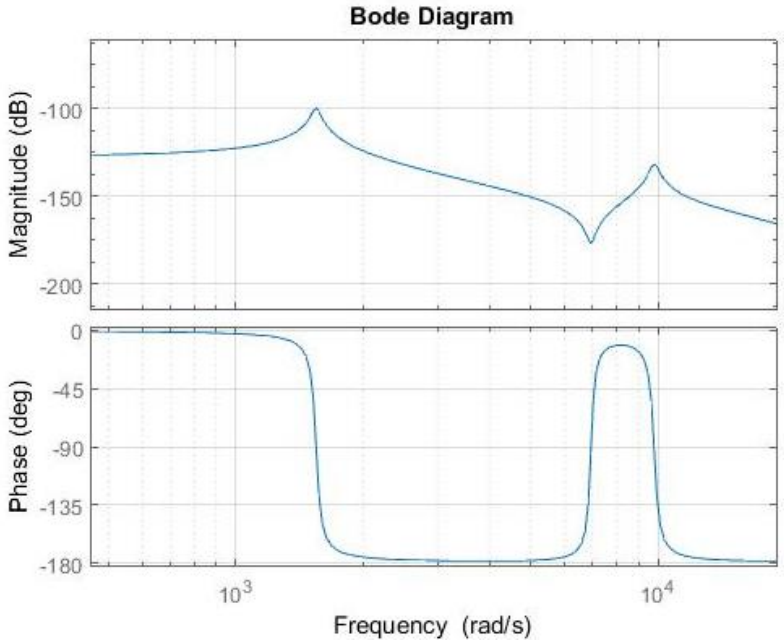

Figure 15: Bode plot for the first two resonant frequencies

Figure 16 displays only the first mode at 247 Hz with the corresponding amplitude of $1.04x10^{-5}$ V.

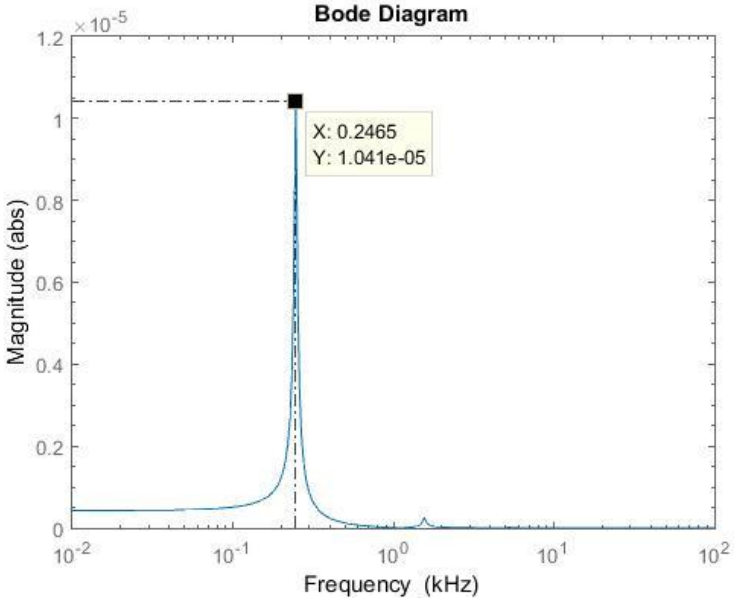

Figure 16: First mode at 247 Hz

The shape of the modes can be better enhanced by increasing the number of elements. Increasing the number of elements will help observe the higher modes and improves the first two modes to have real-like deflection motion. The number of elements is increased to be 10. Figure 17, shows the first mode of the 10 elements case. The first mode shows a smoother deflection than the first case when 2 elements are used and the resonant frequency is the same as well. The difference between the two cases is small and negligible 0%.

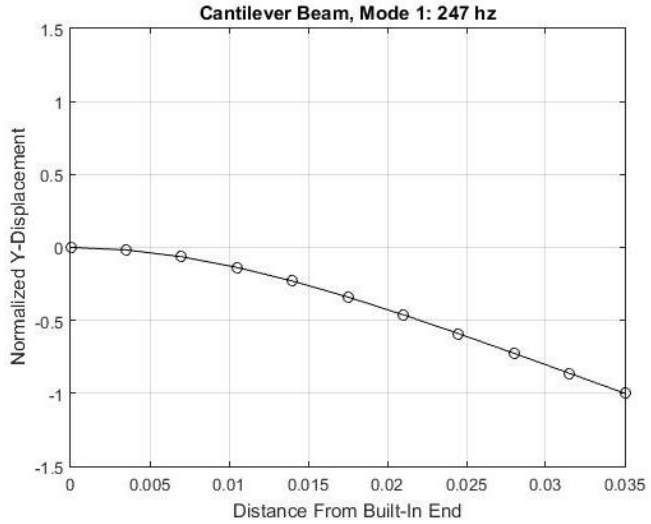

Figure 17: First mode for the 10 elements case

Figure 18, represents the second mode shape of the beam. The second mode is enhanced and the shape is flatter than the case of the 2 elements. Moreover, it has lower resonant frequency than the one of the 2 elements case. And the difference between the two cases is 0.83%.

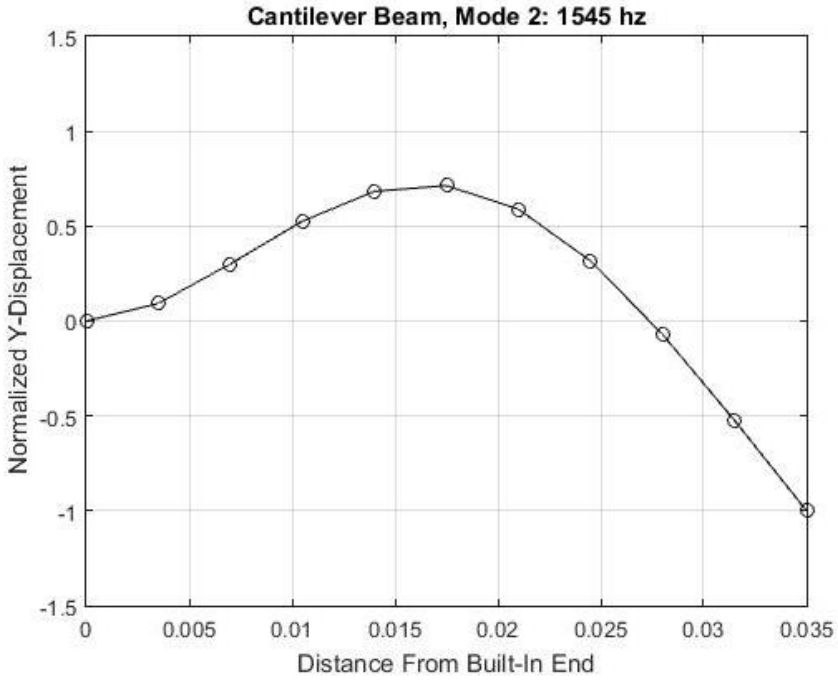

Figure 18: Second mode for the 10 elements case

Figure 19 represents all the modes of the beam and their corresponding resonant frequency when 10 elements are selected.

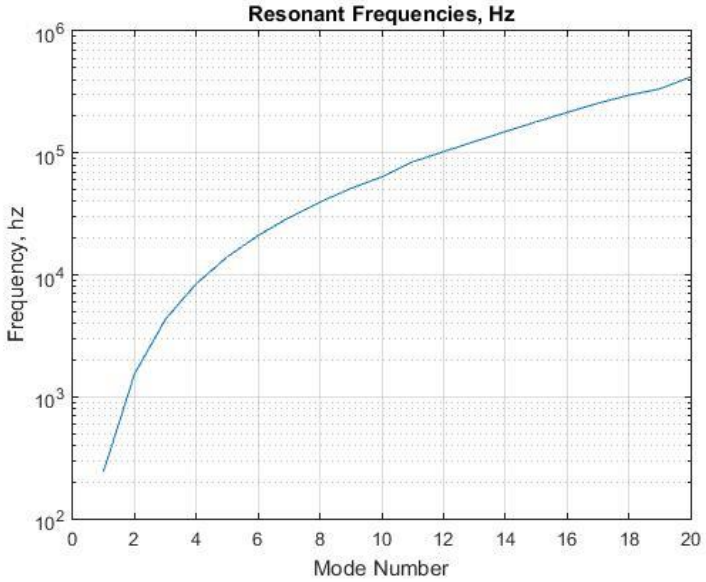

Figure 19: Resonant frequency verses the number of modes

Application of harmonic force at the tip of the beam element results in the highest peak at the resonant frequency as shown in Figure 20. The resonant frequency for the first mode is at 247 Hz. And the second mode appears at 1545 Hz.

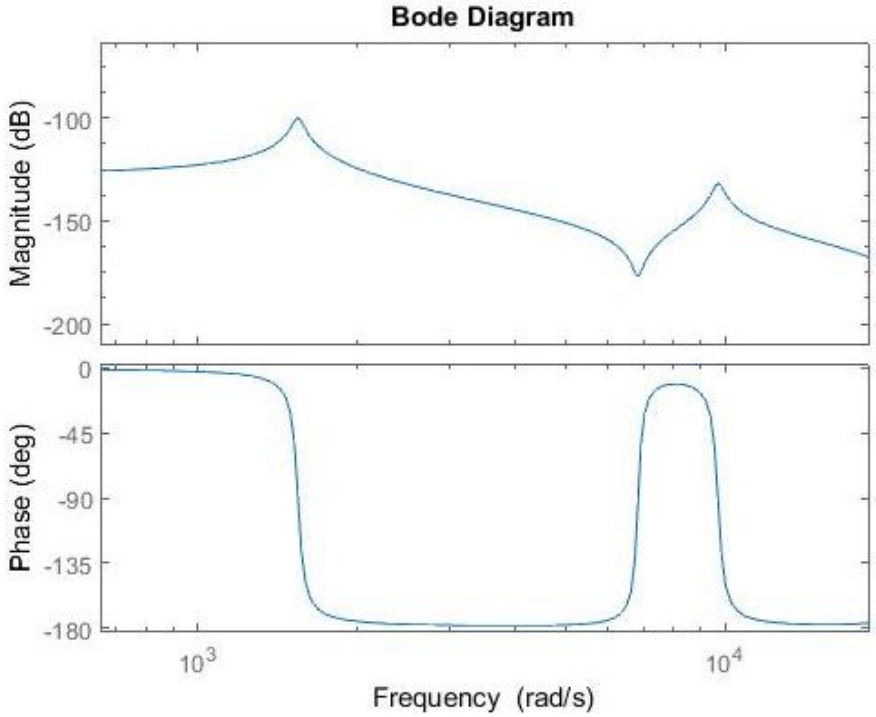

Figure 20: Bode plot for 10 elements case

In conclusion, the first mode for the case of the 2 elements and 10 elements has the same the resonant frequency. While in the second mode, the resonant frequency in both cases is different by 0.83%. Consequently, one can conclude that there is not much difference when using 2 elements or 10 elements and the model would still be valid for both cases. Therefore, the model can be simplified by using 2 elements.

3.5. Theory of the Beam under Free Vibration

The differential equation of a distributed mass along a cantilever beam under free vibration given in equation with the boundary condition given in equation, have mode shapes of the form [50]:

$$X_n(x) = A_n \sin(\lambda_n x) + B_n \cos(\lambda_n x) + C_n \sinh(\lambda_n x) + D_n \cosh(\lambda_n x) \quad (61)$$

Thus the closed form solution of the uniform beam with continuous free vibration for the first two modes is represented as:

$$\omega_n^2 = \alpha_n^2 \sqrt{\frac{EI}{\rho AL^4}} \tag{62}$$

$$\alpha_1 = 1.875$$

$$\alpha_2 = 4.694$$

The natural frequencies are computed for the PZT actuator beam and compared to the mathematical model proposed earlier. In Table 3 the theoretical natural frequencies are compared against the mathematical model and the results are discussed.

Table 3: Comparison between theoretical natural frequencies and the mathematical model

Number of modes	Theoretical natural frequency (Hz) ($F_{theoretical}$)	Mathematical model natural frequency (Hz) ($F_{mathematical}$)	$Error\ \% = \frac{\lvert F_{mathematical} - F_{theoretical} \rvert}{F_{theoretical}} x100\%$
1st	246	247	0.40%
2nd	1545	1545	0%

The percentage of error column in Table 3 shows small difference between the values of the natural frequency of the theoretical results and the proposed mathematical model for 2 elements.

Chapter 4: PZT Design Setup

This chapter verifies the results obtained in the previous chapter through simulation and experimentation. It will be divided into two main sections: the simulation and the experimental work for the PZT design setup. The simulations are carried out using finite element analysis through means of COMSOL Multiphysics software. The details of the experimental setup are also presented in this section. The results and discussion of each section is included.

4.1. Simulation

This section simulates the PZT cantilever beam using COMSOL Multiphysics software. Through this software, the natural frequency of the cantilever beams during vibration can be determined. During vibration, the maximum deflection occurs at the first resonance (natural) frequency. COMSOL uses the finite element method (FEM) analysis to perform the modal analysis. The equations that result from the modal analysis can be viewed as eigenvalues and eigenvector where they represent the frequencies and corresponding mode shapes.

Two dimensional (2D) and three dimensional (3D) simulations of PZT cantilever beams are conducted using COMSOL. The 3D simulation of the cantilever beams is more accurate because it operates in a real world-like manner. 3D simulations are more suitable for nonlinear systems with complex geometry. Those systems are less likely to have closed form solutions. However, the 2D simulations are less computational intensive and have low memory requirements. It also provides fair approximation to the 3D simulation for simple structures.

4.1.1. 3D simulation

The piezoelectric cantilever beams are simulated using COMSOL in 3D and 2D for validation of the results. The first mode of 3D simulation model is shown in Figure 21 and it corresponds to the natural frequency. The natural frequency is found to be 242.16 Hz which can be interpreted as eigenvalue and the bending mode is represented by the eigenvector. An incident wave travelling with 249 Hz deforms the beam the most when compared with the other frequencies.

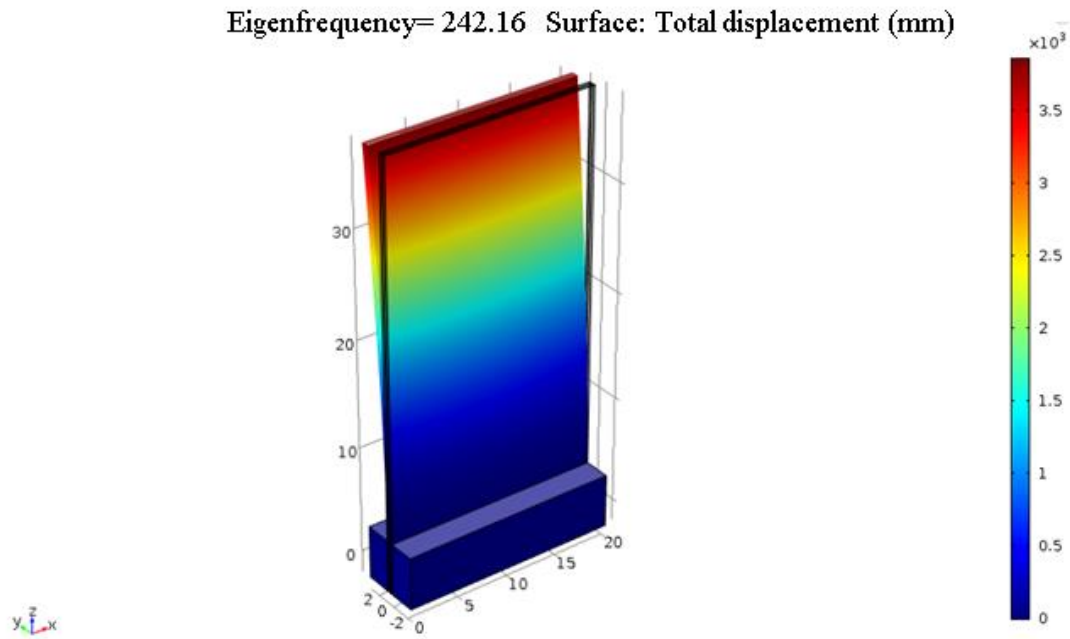

Figure 21: 3D simulation of the first mode (f=242.16 Hz)

In the second mode, the natural frequency occurs at 1543.3 Hz and the corresponding bending mode in 3D simulation is shown in Figure 22.

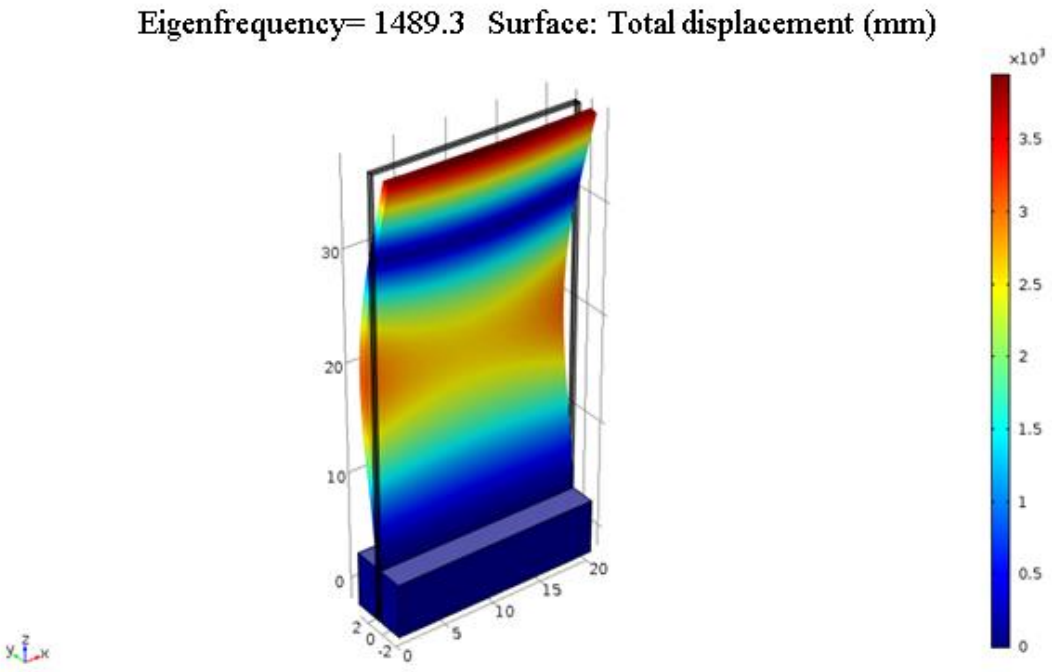

Figure 22: 3D simulation of the first mode (f = 1489.3 Hz)

In comparison with the mathematical model in Eq. 47, the first mode has natural frequency close to the simulation results. The difference between the mathematical natural frequency and the natural frequency of the 3D COMSOL simulation is 1.9%. While the second natural frequency obtained from the mathematical model Eq. 47. is

1545 Hz, the FE simulation resulted in a frequency of 1489.3 Hz. The percentage of error between the simulation results and the mathematical model for the first and second modes are 1.9% and 3.7%. This difference can be reduced by increasing the number of the elements used in the mathematical model. Moreover, this difference is due to the approximated 3D model used in simulation. Table 4 compares the natural frequency from the solution of the differential equation (theoretical model), the proposed mathematical model and the 3D COMSOL simulation.

Table 4: Comparison of the theoretical results, mathematical model, 3D simulation, and percentage of error

Number of modes	Theoretical natural frequency (Hz)	Mathematical model natural frequency (Hz)	3D COMSOL simulation of the natural frequency (Hz)	%Error between mathematical model and 3D Simulation
1st	246	247	242.16	1.9%
2nd	1545	1545	1489	3.7%

4.1.2. 2D simulation

A 2D simulation of the cantilever beam for the first and second mode is shown in Figures 23 and 24, respectively. The first mode is attained at the natural frequency at 249.42 Hz corresponding to the first bending mode. Similarly, the second bending mode occurs at natural frequency of 1543.3 Hz. The 2D simulation results are much closer to the theoretical and the proposed mathematical model. The difference between the mathematical model and the 2D COMSOL simulation for the first mode is 0.8%. The second bending mode is off by the same amount (0.8%) showing that the results are in agreement with the mathematical model.

A comparison of theoretical results, mathematical model and COMSOL simulation results are presented in Table 5. From Tables 4 and 5 it can be seen that the results obtained from 2D and 3D simulations are close to each other.

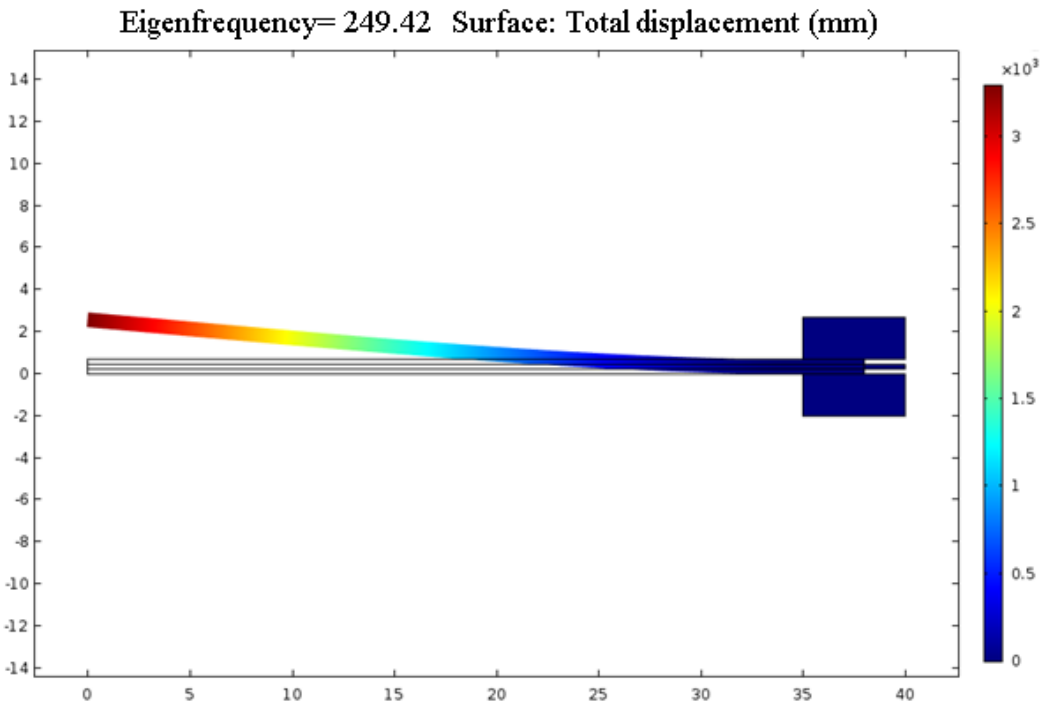

Figure 23: 2D simulation of the first mode (f=249.42 Hz)

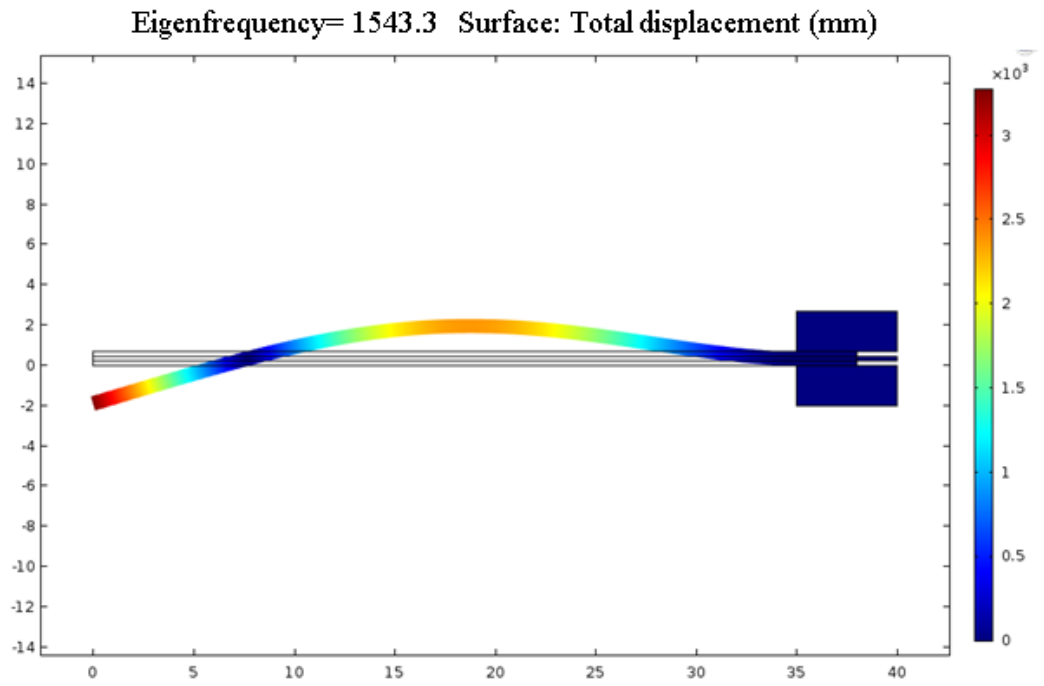

Figure 24: 2D simulation of the second mode (f=1543.3 Hz)

Table 5: Comparison of the theoretical results, mathematical model, 2D simulation, and percentage of error

Number of modes	Theoretical natural frequency (Hz)	Mathematical model natural frequency (Hz)	2D COMSOL simulation of the natural frequency (Hz)	%Error between mathematical model and 2D Simulation
1st	246	247	249	0.8%
2nd	1545	1545	1543	0.8%

The aforementioned 3D simulations results are closer to the mathematical model. Also, the 2D simulation result is close approximation to the 3D and is less computationally expensive. Therefore, the 2D COMSOL simulation can be used instead of the 3D. Moreover, the small difference between the 3D COMSOL simulation and the mathematical model can be attributed to the fact that COMSOL software uses large number of elements, while the mathematical model uses only 2 elements to represent the system. In conclusion, the proposed mathematical model gives good approximation to the simulation results.

4.2. Experimental Apparatus and Results

The experimental setup and the recommended methodology to harvest energy from acoustics using dual PZTs are presented in this section. A PZT setup is designed to validate the simulation and mathematical models. The proposed methodology improves the energy harvested in comparison with previous studies [6, 9]. The resonant (natural) frequency of the system is experimentally obtained. It is shown that the experimentally obtained system frequency agrees with the mathematical model derived in chapter 3. The obtained energy from the dual PZT is amplified using quarter-wavelength resonator tube. The design, manufacturing and tube testing is completed and the results are discussed in Chapter 5. The block diagram of the experimental setup is shown in Figure 25.

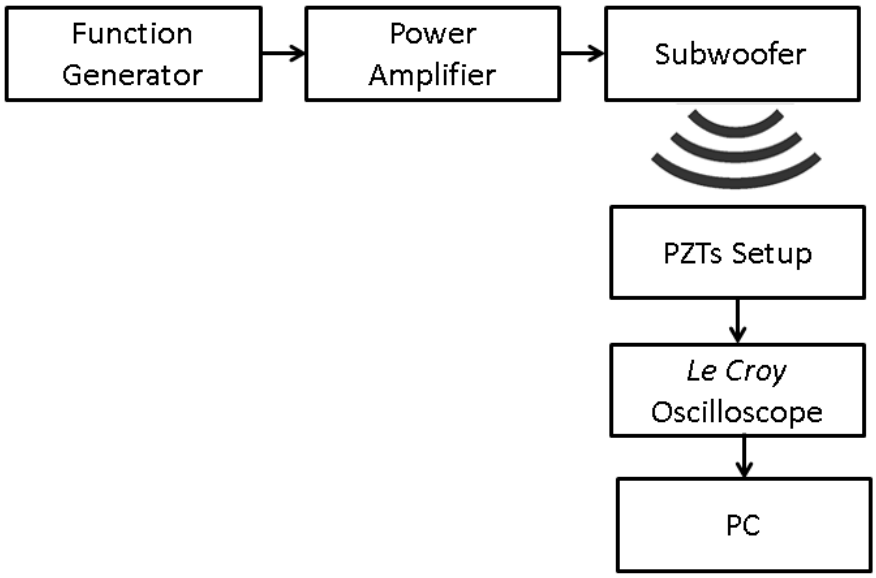

Figure 25: Block diagram for experimental setup

A TG550 function generator produces a sine wave which will be driven by a Crown XLS 1000 DriveCore Series power amplifier (by Harman) to amplify the subwoofer speaker (JBL JRX118S 18 in Compact Subwoofer). The PZT design setup is placed in front of the subwoofer and the data is collected through *Le Croy* oscilloscope connected to a computer (PC).

The design of the dual PZTs setup uses two single PZT plates to harvest energy. It consists of two steel plates that aim to wrap the two PZTs. The two single bimorph PZT piezoelectric plates (model Stripe Actuator 40-2010) are used. The steel plates are cleaned and well-polished to allow perfect enclosure when tightened with nuts and bolts. An insulating tape is covering both steel plates from the inside to prevent short circuit between them and allow harvesting data without any complication. The design was fixed on two metal rods with a base that was on top of a table facing the subwoofer. Figure 26 illustrates the dual PZTs setup system.

The intended sound of our interest is of a low frequency. The subwoofer produces a low frequency sound wave that can be used to simulate the real life sound waves. The piezoelectric system can be placed in front of the speaker at different distances based on the following equation:

$$\lambda = \frac{v}{f} \tag{63}$$

where λ is the wavelength of the sound wave, v is the speed of the sound and f is the frequency.

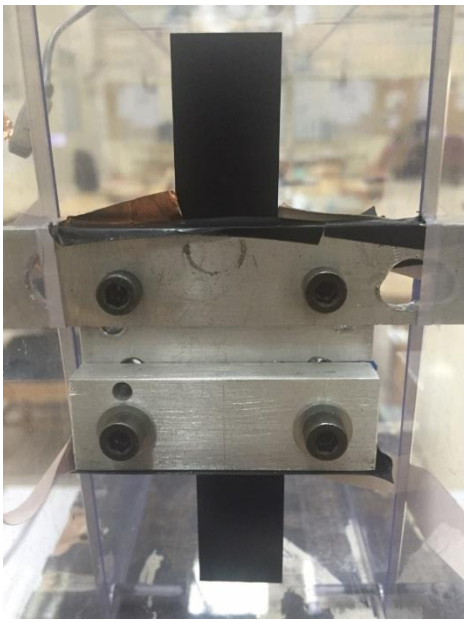

Figure 26: The PZT design setup

A subwoofer is employed along with an amplifier and function generator to generate an incident wave. The sound pressure level (SPL) of the incident wave is found through employing a microphone. A quarter-inch microphone (model 377C10 manufactured by PCB Piezotronics) is used. The pressure output from the subwoofer is calculated through the following equation:

$$Pressure\ (Pa) = \frac{Voltage\ (mV)}{Sensitivity\ (\frac{mV}{Pa})} \tag{64}$$

where S is the sensitivity of the microphone and it is (1 mV/Pa)
Then the SPL is calculated as follows:

$$SPL = \left(20 \log\left(\frac{Vrms}{S\ Pref}\right)\right)\ dB \tag{65}$$

where P_{ref} is the reference pressure in the air which is 20 µPa [26].

The function generator is connected to the subwoofer to generate sound waves of specific frequency and amplitude. The maximum frequency the subwoofer can tolerate is 250 Hz according to the subwoofer manufacturing datasheet thus the maximum wavelength can be calculated as:

$$\lambda = \frac{v}{f} = \frac{343.2\ m/s}{250\ Hz} = 1.37\ m$$

There exists a full wavelength of the sound wave at the 250 Hz when placed at 1.37 m. However, there does not exist an insulated area i.e. anechoic chamber to prevent the background noise interfering the subwoofer sound waves. Therefore, the experimental setup is placed close to the subwoofer to minimize the noise and error.

Both the voltage produced by the deformed cantilever PZT plate and the frequency of the function generator are measured and recorded. Natural frequencies of both of the PZTs are determined and to be compared with the mathematical model. The function generator generated sine wave with amplitude of $2V_{pp}$ and the frequency is varied between 190-250 Hz. The incident wave SPL is calculated using Eq. 62:

$$SPL = \left(20 \log\left(\frac{Vrms}{S\ Pref}\right)\right) dB$$

$$SPL = \left(20 \log\left(\frac{2.7x10^{-8}}{1mV * 20\mu}\right)\right) = 101\ dB$$

The incident sound pressure level is 101dB.

Then the frequency is ranged to find the natural frequency of dual piezoelectric cantilever beams at SPL of 101 dB. The experimental apparatus is shown in Figure 27 with all equipment used. The experimentation is conducted in the Mechatronics lab.

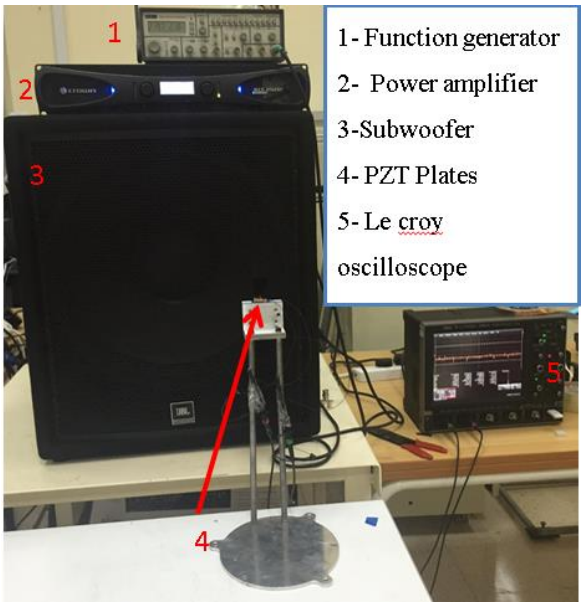

Figure 27: Experimental Setup

For testing purposes, one PZT plate is investigated to verify the natural frequency. The output voltage of the PZT plate is first observed in *Le croy* oscilloscope

while changing the frequency. The highest amplitude sinusoidal signal is observed at 239 Hz in the time domain. The data of the output voltage is then plotted in MATLAB to view the natural frequency of the single PZT (See Figure 28).

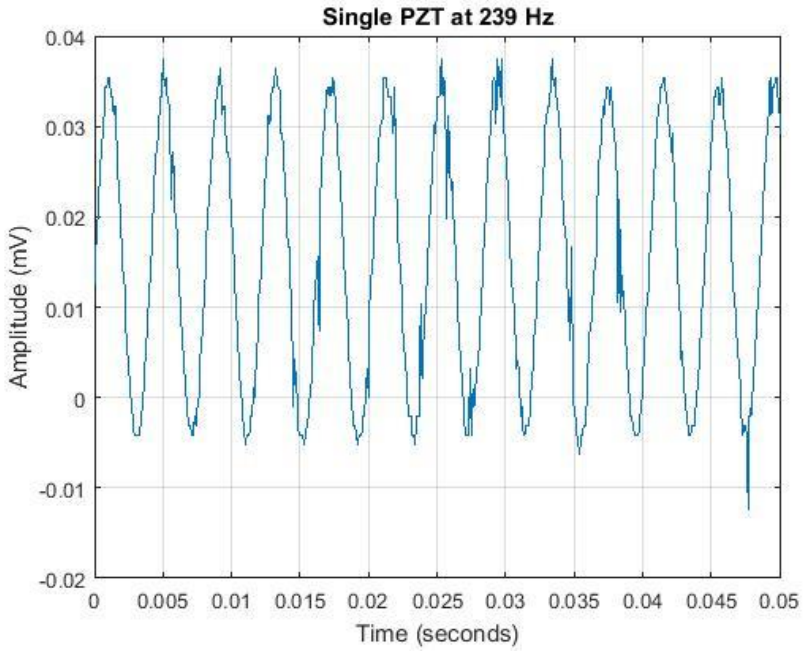

Figure 28: Time domain signal at 239 Hz in MATLAB

The Fast Fourier Transfer (FFT) plot proved that the resonant frequency is 239 Hz which is close to 242.16 Hz of the simulation results in 2D. As shown in Figure 29 the natural frequencies differ by 1.3%. Also, the experimental results are different from the mathematical model by 3.2%.

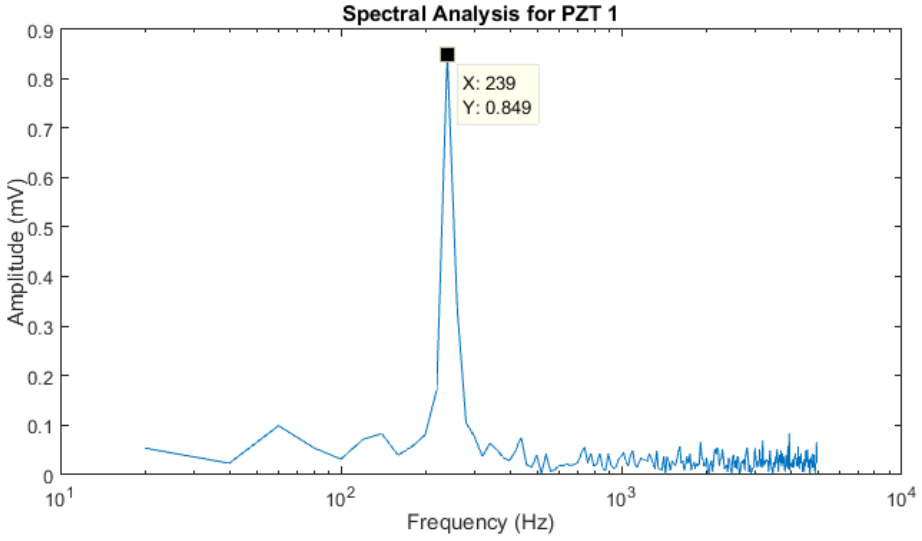

Figure 29: Spectral analysis of single PZT

One can observe that the percentage of error is minor and the simulation matches the experimental results. The small percentage of error indicates that the design works fine. The amplitude can be further amplified through the tube resonator.

Next, an experimental setup using the two PZTs was to be realized. One PZT plate is fixed upward and the second one downward where both are facing the center of the subwoofer. The orientation of the PZT plates is made in such a way it doubles the energy harvested when compared to one PZT plate.

Figure 30, shows the output of both PZTs actuators. The yellow signal represents the upper PZT (C1) and the red signal (C2) represents the lower PZT. Both PZTs produce almost the same wave signals with almost identical amplitude. The reason behind the small difference could is due to the incident waves on the two PZTs. To further minimize the difference the bulky steel design can be optimized and reduced to have both PZTs closer to each other. The natural frequencies for the upper and lower PZTs are at 239 Hz and almost the same as the simulation results and close to the mathematical model.

The percentage of error is the same for both PZTs that is 1.3%. There are many factors involved that affect the harvesting process; one of them is that the combinations of free length, thickness, width, and the applied voltage play huge role in the resulting resonant frequency. Since the resonant frequency is function of length of the PZT. The resonant frequency could be changed according to the free length of the PZT that is not securely clipped within the steel plates. In other words, more of the length of the PZT plate should be clamped. The highest peak was found at 239 Hz and the FFT was done in Figure 29. The natural frequency can be better enhanced by allowing the free length of the PZT to be inserted more within the steel plates. There exists an inverse relationship between the free length and the natural frequency of the PZT system.

The sine waves of both PZTs were plotted in MATLAB to verify the results and to obtain the FFT. Figure 30 shows the signals in the time domain at 239 Hz.

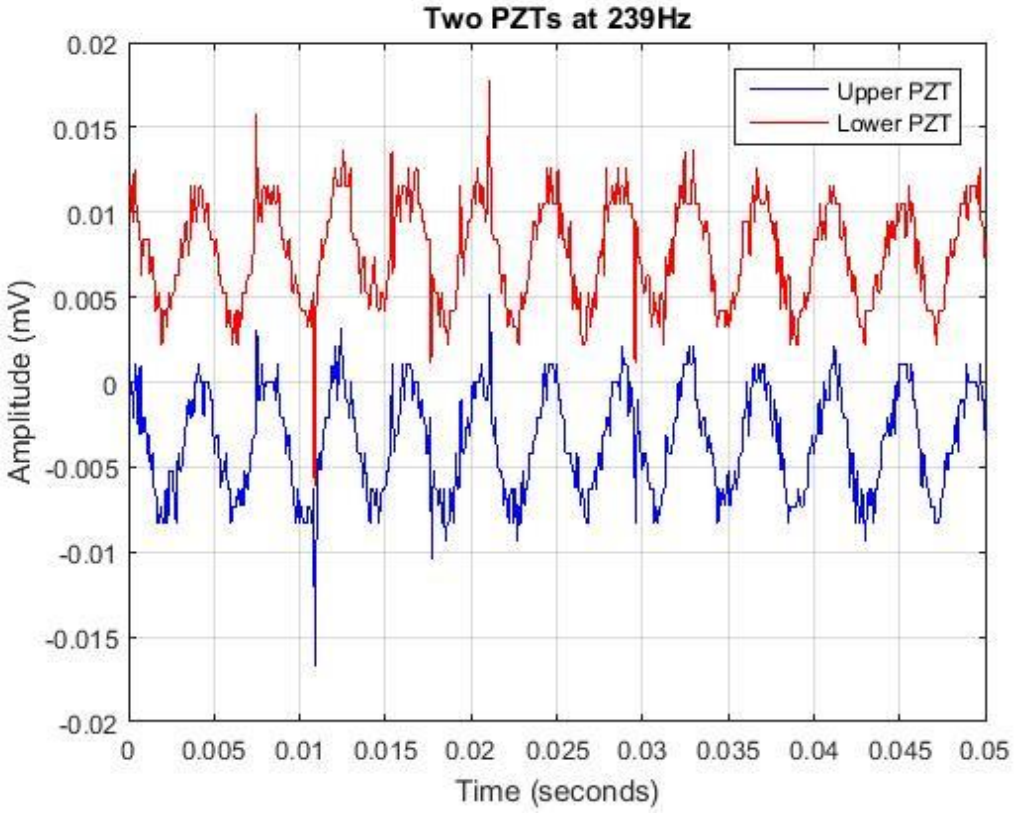

Figure 30: Both PZT signals in time domain at 239 Hz in MATLAB

The FFT of both signals is presented in Figure 31 and Figure 32 respectively. The highest peaks of both PZTs is at 239 Hz, however, there is small difference in the amplitude of the PZT signals. The first PZT (Lower PZT) has amplitude of 0.849 mV while the second PZT has amplitude of 0.8969 mV (Upper PZT).

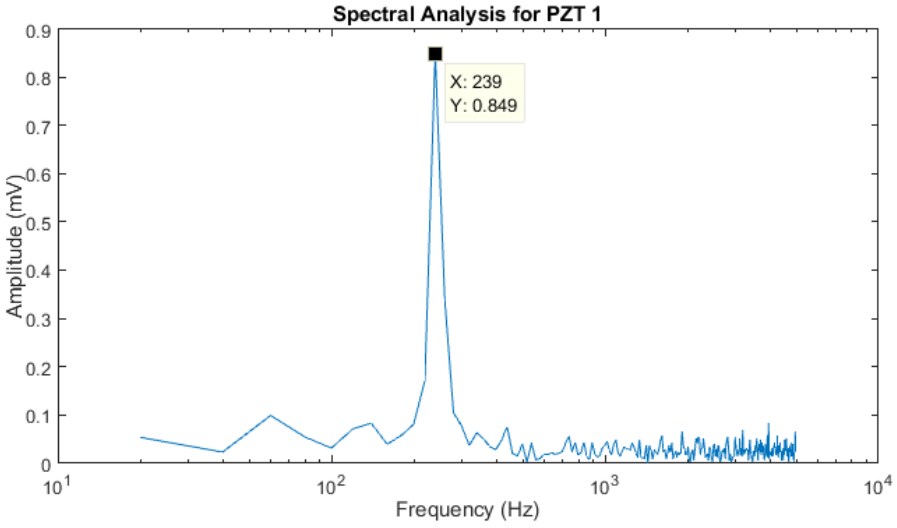

Figure 31: Spectral analysis of the lower PZT at 239 Hz

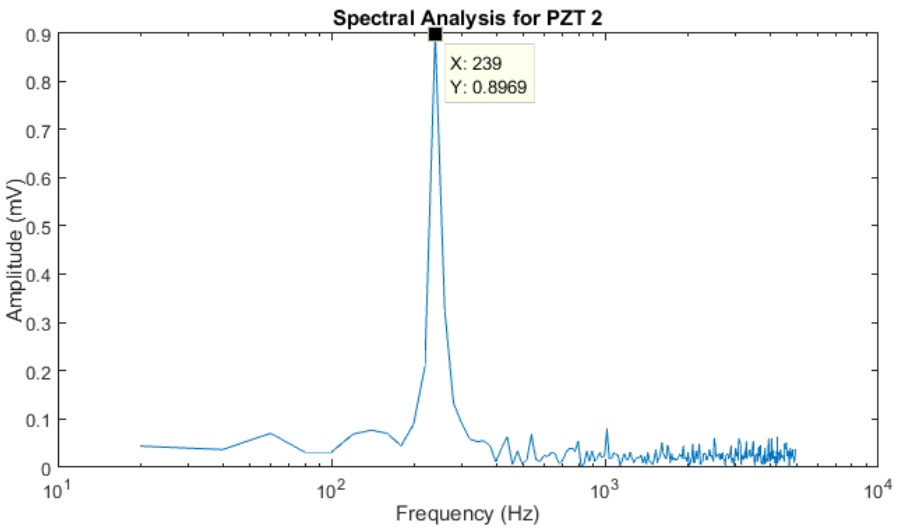

Figure 32: Spectral analysis of the upper PZT at 239 Hz

This small difference in the peaks can be due to the orientation position of each of the PZTs. Another reason could be because of the size of the steel plates sandwiching the PZT plates where it can be reduced to smaller dimension to have incident waves directed to the PZTs cantilevers as much as possible.

Moreover, the output voltage can be increased when the SPL is increased. An increase of the incident SPL =114 dB produces an output voltage of 3.701 mV as shown in Figure 33. In comparison with Figure 31 and Figure 32 when the incident SPL = 101 dB at the natural frequency showed lower output voltage than the case of SPL = 114 dB. Thus one can conclude that there exists a relationship between the increase of SPL and output voltage.

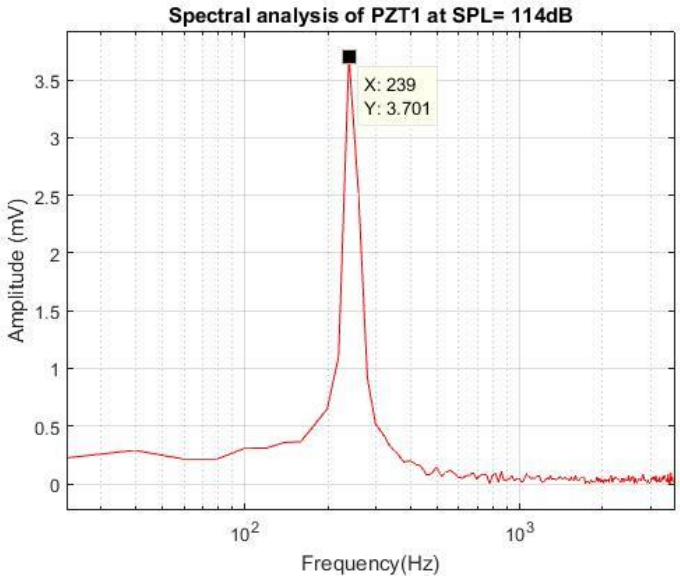

Figure 33: Voltage output of PZT at SPL=114 dB

Moreover, the results of the experimental data are compared to the mathematical model formulated in Chapter 3. The natural frequency found through experimentation showed high resemblance to the mathematical model's natural frequency. The natural frequency from the experiment is found to be 239 Hz while the one obtained from the mathematical model is 247 Hz; i.e. a difference of 8 Hz which indicates that the mathematical model is in close agreement with the experimental results. The natural frequency acquired experimentally and the one attained mathematically are plotted in Figure 34.

To further increase the total output voltage from the PZT plates; the plates can be placed within a tube resonator. The design procedure of the tube resonator is discussed in Chapter 5.

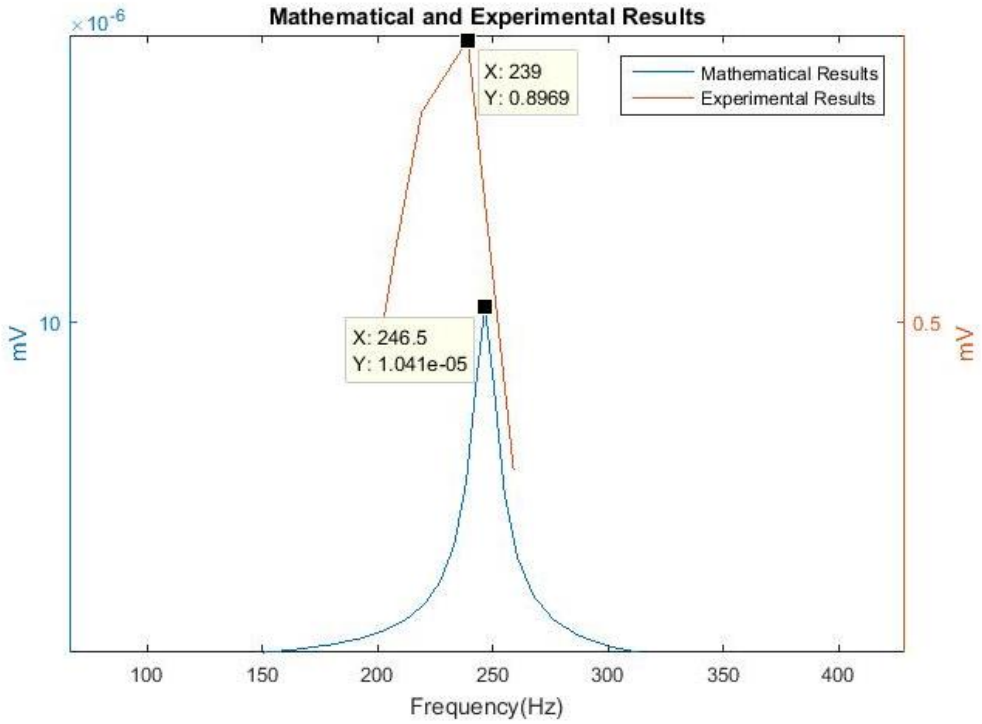

Figure 34: Mathematical and the experimental results

Chapter 5: Tube Resonator

In this chapter, the PZT design setup built previously will be used to amplify its output voltage through a quarter-wavelength tube resonator. The process of designing the tube resonator in simulation is described in details. After determining the length of the tube from the simulation it was preceded to manufacturing. Then different tests were carried on with the tube in which all of them are discussed in details.

5.1. Simulation

A straight acoustic tube resonator with PZT piezoelectric plates is designed to amplify the energy harvested from the PZT design setup. Simulation is first accomplished through COMSOL Multiphysics to identify the length of the tube resonator. The length of the tube depends on the previously obtained natural frequency of the system. First the dimensions of the tube resonator are considered according to the dimensions of the designed PZT setup. A width of 0.07 m and height of 0.15 m were defined with inclusion of tolerance. The length of the tube is calculated using COMSOL with the succeeding equation:

$$f = \frac{c}{4 * (L + 0.4 * d)} \tag{66}$$

where c is the speed of sound, L is the length of the tube, d is opening diameter, f is the resonant frequency

Re-arranging the equation to solve for the length L:

$$L = \frac{c}{4 * f} - 0.4 * d \tag{66.a}$$

A tube resonator of length 0.3587 m is chosen after many trials to get the natural frequency as close as possible to the one obtained experimentally through simulation. The natural frequency changes with the change in the length of the tube. Figure 35, shows a vertical line from the simulation is very close to the resonance frequency from the experimental results 239 Hz.

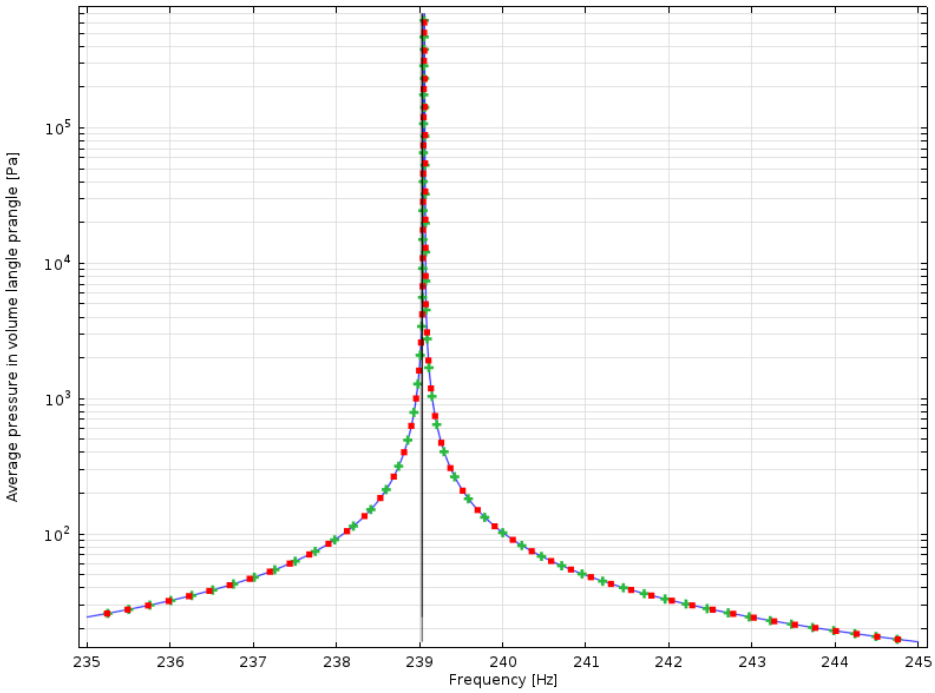

Figure 35: Comparison between experimental results and simulation

5.2. Experimental Apparatus and Results

Based on the simulation, the quarter-wavelength straight tube resonator is manufactured with dimensions, $0.07 \times 0.15 \times 0.3587\ m$ and half inch polycarbonate material. Figure 36 displays the tube open from one end and closed from the other.

Figure 36: Perspective view of quarter-wavelength tube resonator

The tube is adjusted to fit the PZT system which is placed in the centerline and 0.05 m away from the open inlet. This is due to the fact that the pressure gradient is maximum at a distance of 0.05 m from the inlet, hence a large displacement of the plates will occur causing high voltage generation [9]. From [8], it should be noted that the

piezoelectric plates are set starting from the open inlet and successively placed towards the closed end of the tube. Thus, the first plate at the open inlet will generate the highest voltage relative to the other plates. Therefore, in this design dual piezoelectric are placed closer to the open inlet to double the voltage generated.

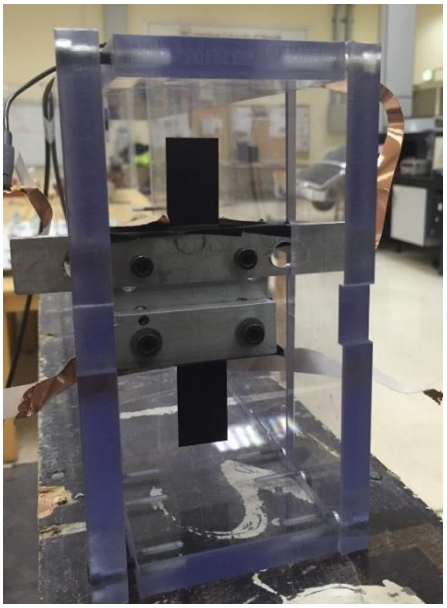

Figure 37: Front view of quarter-wavelength tube resonator with PZT plates

Afterward, the quarter-wavelength tube resonator is placed on top of base constructed of wood to have rigid support. Also, the wooden base will absorb any external vibration that might interfere with the acoustic vibration from the subwoofer. The height of the wooden base is such that the tube resonator is facing the subwoofer in the middle.

Figure 38: Experimental setup

Furthermore, similar to the experiment conducted in Chapter 4, the function generator will supply the amplifier of the subwoofer thereby the generating sound at low frequency. The wave sound will travel through the tube resonator across the PZT system to ensure that the tube is excited at the resonance frequency. The experimental setup for the overall system with the tube is shown in Figure 38.

5.2.1. Results and Discussion

For testing, a single PZT is placed inside the tube resonator to verify the amplification that the tube causes. Figure 39, shows the simulation results of the single PZT.

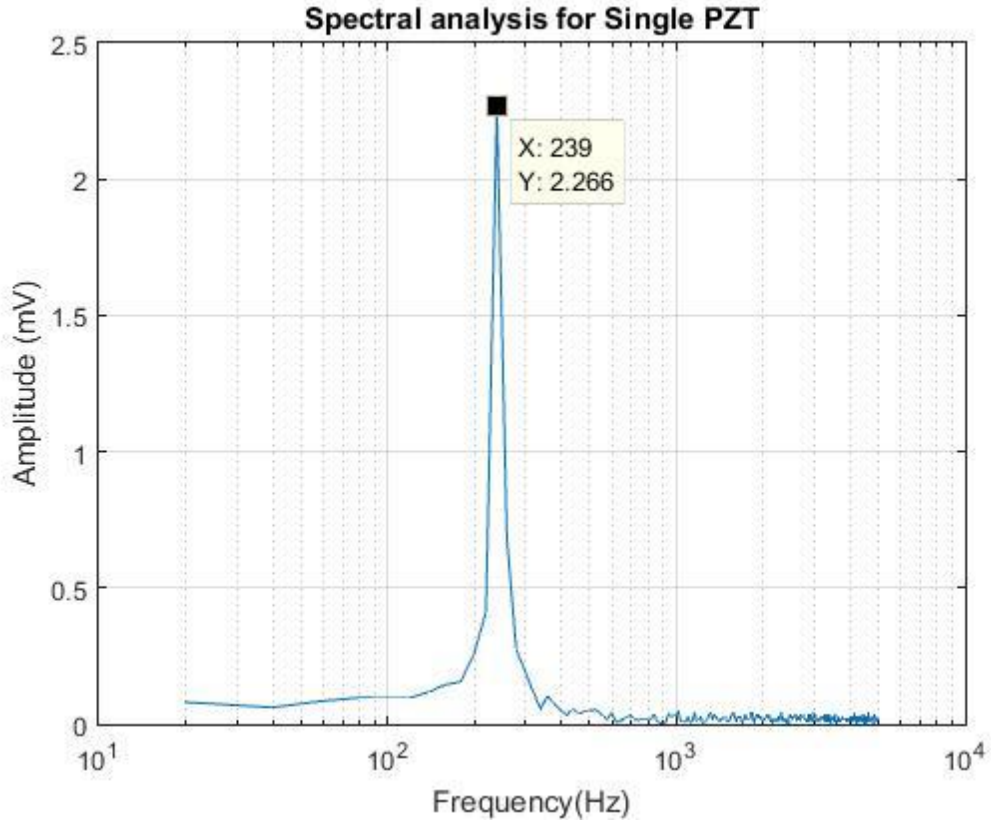

Figure 39: Single upper PZT inside the tube

The peak is found to be at the resonant frequency (239 Hz). The peak is amplified and it is 2.266 mV compared to the results obtained earlier without the tube there is an increase of 1.3691.

Afterward, the two PZTs are placed within the tube in the aforementioned distance. Then, the subwoofer was operated 239 Hz resonant frequency. Figure 40, represents the upper and lower voltage output from the PZTs. It is noticed that the upper

PZT produces more voltage than the lower one. The voltage output of the upper and lower PZTs are 2.105 mV and 1.784 mV respectively.

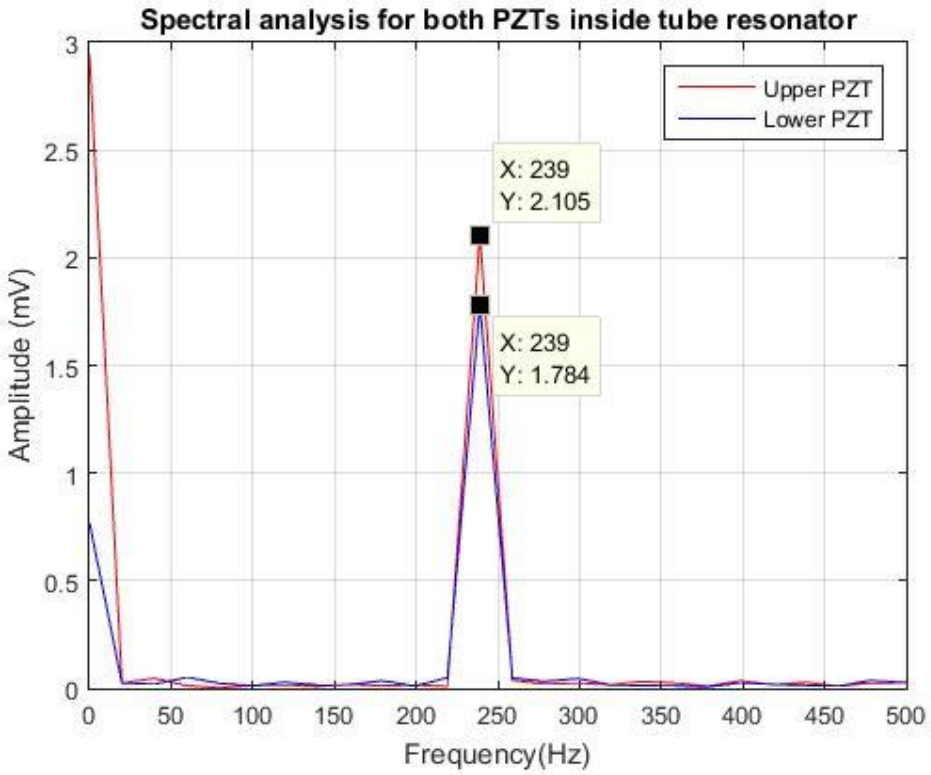

Figure 40: Spectral analysis of the PZTs inside the tube

The input voltage from the function generator is 2.20 V_{pp} that is 1.09 V is the supplied voltage to the subwoofer. However, the input voltage to the upper PZT is 1.35 mV measured through the aforementioned microphone device. Therefore the amplification ratio can be calculated as:

$$Amplication\ ratio = 20\log(\frac{V_o}{V_{in}}) \quad (67)$$

where Vo is the output voltage and Vin is the input voltage

$$Amplication\ ratio = 20xlog\left(\frac{2.105\ mV}{1.35mV}\right) = 3.85dB$$

The fact that the PZTs output voltage is higher than the input voltage means that the tube resonator amplified the voltage at the resonant frequency (239 Hz). Similarly, the amplification ratio is calculated for the lower PZT and it is 2.411 dB.

5.3. Multiple Tests

Placing the PZT plates inside the tube resonator changes the resonance behavior of the tube. The reason behind the change of behavior is due to the disturbance of motion of the air particles inside the tube. Therefore, a test to ensure the tube is excited at the resonant frequency. The incident frequency inside the tube is swept to observe the output voltage. The frequencies ranged from 230-250 Hz. The results are tabulated in Table 6 which represents the frequency and the corresponding amplitude for the upper PZT.

Table 6: Frequency Vs. Amplitude for PZT1

Frequency (Hz)	Amplitude (mV)
233	1.275
239	2.341
243	2.244
253	1.861

Then using MATLAB the range of frequnices along with their amplitudes are plotted as shown in Figure 41.

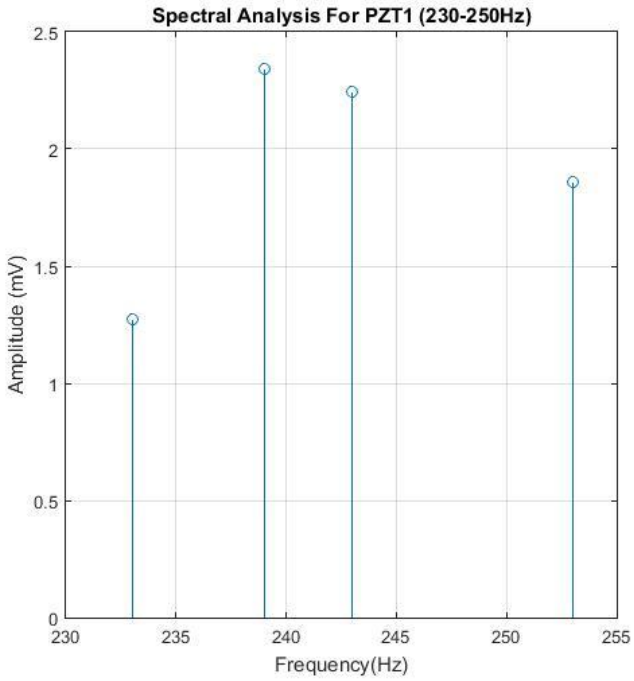

Figure 41: Frequencies Vs. Amplitude for PZT 1

Figure 41 verifies that the maximum output voltage is achieved at the resonant frequency. In other words, the structural resonant frequency of the PZT plate is matching the acoustic resonant frequency of the tube where the maximum energy harvesting occurs. The harnessed electricity is generated at d_{31} mode.

Similarly, for PZT 2, the incident frequency is ranged from 230-250 Hz. The incident frequency and the corresponding amplitude is recorded in Table 7 and plotted in Figure 42.

Table 7: Frequencies and the amplitudes of PZT2

Frequency (Hz)	Amplitude (mV)
233	1.293
239	1.784
243	1.633
253	1.614

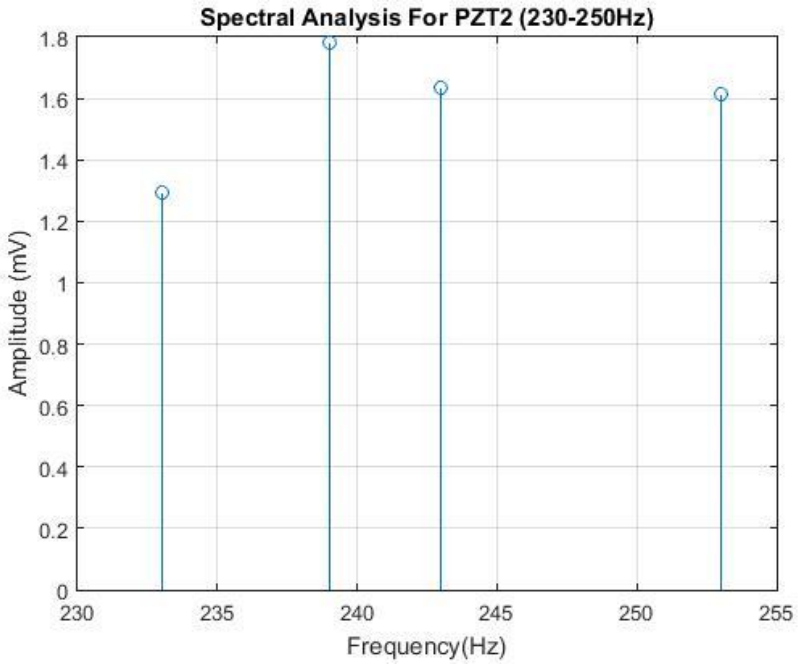

Figure 42: Frequency Vs. Amplitude for PZT2

It is noticed that the resonant frequency produces the highest voltage inside the tube and that means the tube resonator is manufactured accurately.

Then, the experimental data were plotted against the mathematical model. Figure 43, shows that the resonant frequency of the mathematical model at 247 Hz while the experimental resonant frequency is at 239 Hz. Both of the plots show that the resonant frequency produces the highest voltage.

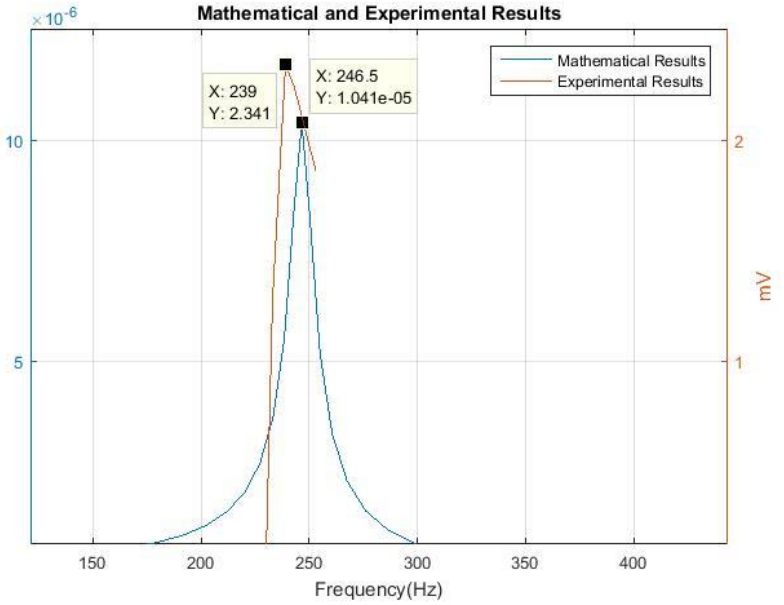

Figure 43: Comparison between the mathematical results and the experimental

5.4. Testing with 1 meter distance

For practical applications, the PZTs will not be placed directly near the sound source but rather in appropriate distant location. Therefore, in this study the tube resonator along with the PZT plates within is located 1 meter away from the subwoofer. The experimental setup is then modified by moving the tube resonator 1 meter from the subwoofer as seen in Figure 44.

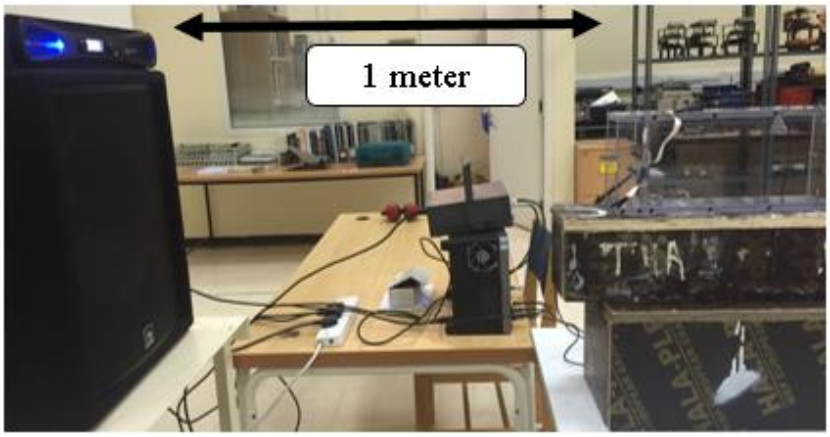

Figure 44: Experimental setup with 1 meter distance

The same test to evaluate the maximum voltage at resonant frequency is conducted. The resonant frequency at 239 Hz for the individual PZTs generated voltage of 1.75 mV and 0.635 mV. The generated voltage is lower than that when the tube was closer to the subwoofer. This is due to the fact that the acoustic waves are not fully transmitted to the piezoelectric plates but rather lost in the air. In comparison with the case of the tube being near the subwoofer the waves were directed to the PZT plates thus the maximum amount of sound was absorbed. However, the generated voltage is still higher when comparing it to the results found without the tube. This means the tube works well as an amplifier when compared to the case of the PZT plates without the tube.

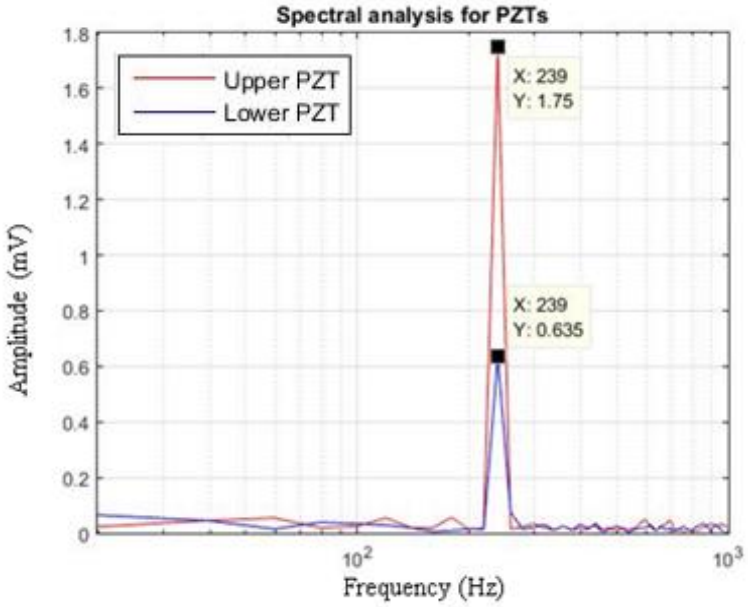

Figure 45: Spectral analysis for the dual PZT plates

Through experimentation, the lower PZT is noticed to give less voltage than the upper PZT, a difference of 1.115 mV between the lower and upper PZT.

5.4.1. Multiple Testing with 1 meter distance:

A test for the PZTs within the tube that is 1 meter away from the subwoofer is conducted. This is done to verify that the incident wave natural frequency matches the tube resonator natural frequency. Figure 46 demonstrates the various frequencies and their corresponding amplitudes.

Compared to Figure 41, the amplitudes are lower than when the tube was closer to the subwoofer by 1.6156 mV.

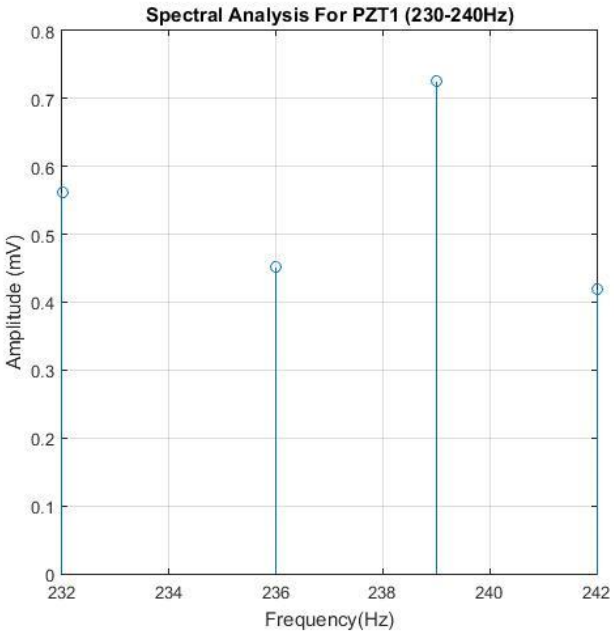

Figure 46: Frequency Vs. Amplitude for PZT1

Furthermore, the amplitude of the resonant frequency is still the highest. The data of the frequencies and their corresponding amplitudes are tabulated in Table 8 .

Table 8: Range of frequencies and their amplitudes for PZT1

Frequency (Hz)	Amplitude (mV)
232	0.561
236	0.4512
239	0.7254
242	0.4189

Similarly, the second lower PZT is interfaced with various ranges of frequencies from 230-240 Hz. This is done to verify the operation of the tube resonator and the resonant frequency is found to be at 239 Hz. Figure 47 shows the frequencies and their corresponding amplitudes of the second PZT.

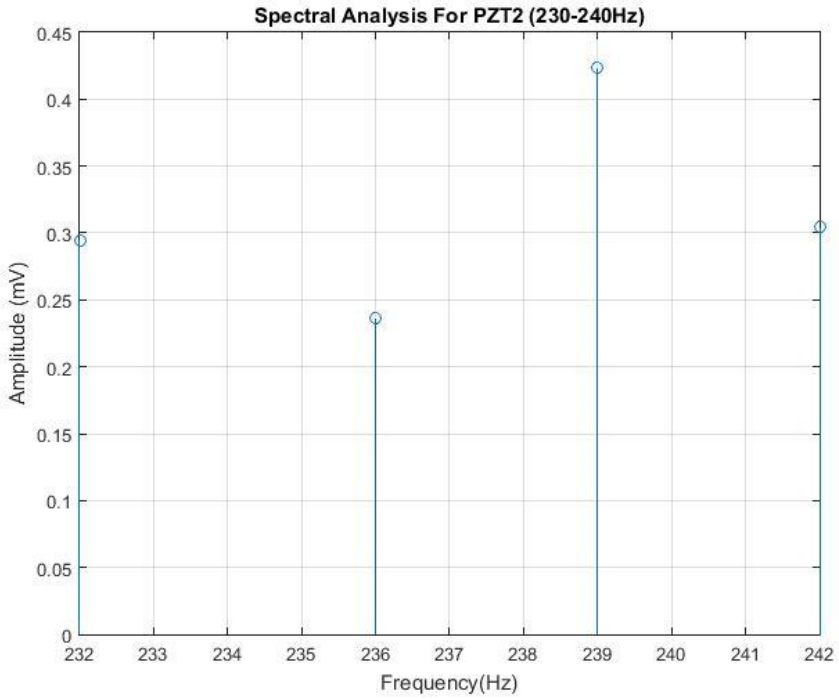

Figure 47: Frequency Vs. Amplitude for PZT2

Table 9 represents the output amplitude of the second PZT which have lower amplitude than the first PZT.

Table 9: Range of frequencies and their amplitudes for PZT2

Frequency (Hz)	Amplitude (mV)
232	0.2948
236	0.2362
239	0.4239
242	0.3047

The tube resonator has shown fair amplification ratio when it was used near and 1 meter away from the subwoofer. Therefore, it can be used to amplify the output voltage from the PZT plates. The tube resonator worked quite well due to the proper dimension choice.

Chapter 6: Conclusions and Future Work

A low frequency acoustic energy harvesting setup using dual PZTs is designed. This design has not been recorded in the energy harvesting field. It will be used to convert sound/vibrational energy into voltage to power low-power electronic devices. This research focuses on developing a new method to harvest maximum energy from the surrounding acoustics at low frequencies such as airplanes, factories and car traffic noise. A mathematical model was first established to evaluate the natural frequency of the system and the different corresponding modes. Theses natural frequencies and modes were validated through a simulation model employing FEA methods through means of the COMSOL Multiphysics software. The simulation results provided natural frequency that is close to the mathematical model. The natural frequency for the PZTs is 242 Hz in simulation and 247 Hz from the mathematical model. The natural frequency was then verified using experimentation.

The natural frequency and its corresponding output voltage harvested are then amplified using quarter-wavelength straight-tube resonator. The PZT plates are placed within the straight quarter-wavelength tube resonator that is manufactured according to the natural frequency attained. The output voltage is almost double the input voltage. The amplification ratio is 3.85 dB at the resonant frequency (at 239 Hz). Multiple tests were conducted when the tube resonator was located near and 1 meter away from the subwoofer. Those tests were studied and the conclusion can be drawn that the further the sound source from the PZT the less the energy harvested.

Future work will come in the form of reducing the size of the PZT design to be more compatible and efficient. The bulky design of the PZT inside the tube will allow the acoustic travelling waves to directly be in contact with the PZT plates. Furthermore, accurate capture of the natural frequency can be achieved by finding a fixed way to mark the free length of the cantilever PZT and thus changing it accordingly. Also, the experiments could be conducted in an isolated room where the sound will be absorbed completely i.e. anechoic chamber. Also, conducting the tests in cold environment will help produce more energy.

Moreover, the PZT design can be altered in such a way so that the PZT cantilever plates are mechanically coupled. This will allow the PZT plates to have two natural frequencies by employing the two vibration modes (rocking and bending).

References

[1] S. B. Horowitz, M. Sheplak, L. N. Cattafesta, and T. Nishida, “A MEMS acoustic energy harvester,” *Journal of Micromechanics and Microengineering*, vol. 16, no. 9, pp. 174-181, Sep. 2006.

[2] F. Liu, S. Horowitz, T. Nishida, L. Cattafesta, and M. Sheplak, “A multiple degree of freedom electromechanical Helmholtz resonator,” *The Journal of the Acoustical Society of America*, vol. 122, no. 1, pp. 291–301, April 2007.

[3] F. Liu, A. Phipps, S. Horowitz, K. Ngo, L. Cattafesta, T. Nishida, and M. Sheplak, “Acoustic energy harvesting using an electromechanical Helmholtz resonator,” *The Journal of the Acoustical Society of America*, vol. 123, no. 4, pp. 1983–1990, April 2008.

[4] S. Kim, C. Ji, P. Galle, F. Herrault, X. Wu, J. Lee, C. Choi, and M. G. Allen, “An electromagnetic energy scavenger from direct airflow,” *Journal of Micromechanics and Microengineering*, vol. 19, no. 9, pp. 133-136, Aug. 2009.

[5] M. Lallart, D. Guyomar, C. Richard, and L. Petit, “Nonlinear optimization of acoustic energy harvesting using piezoelectric devices,” *The Journal of the Acoustical Society of America*, vol. 128, no. 5, pp. 2739–2748, Nov. 2010.

[6] B. Li and J. H. You, "Harvesting ambient acoustic energy using acoustic resonators," in *Proceedings of Meetings on Acoustics 161ASA*, vol. 12, no. 1, pp. 397-405, May 2011.

[7] Vatansever D, Hadimani RL, Shah T and Siores E, “An investigation of energy harvesting from renewable sources with PVDF and PZT”, *Smart Materials and Structures*, vol. 20, no. 5, pp. 964-972, April 2011.

[8] B. Li, A. J. Laviage, J. H. You, and Y.-J. Kim, “Harvesting low-frequency acoustic energy using quarter-wavelength straight-tube acoustic resonator,” *Applied Acoustics*, vol. 74, no. 11, pp. 1271–1278, Nov. 2013.

[9] K. Li, J. You and K. Yon-Joe, "Low frequency acoustic energy harvesting using PZT piezoelectric plates in a straight tube resonator," *Smart Materials and Structures*, vol. 22, no. 5, pp. 964-1726, May 2013.

[10] B. Li and J. H. You, "Simulation of Acoustic Energy Harvesting Using Piezoelectric Plates in a Quarter-wavelength Straight-tube Resonator," *Proceedings of the 2012 COMSOL Conference, Boston, USA*, April 2012.

[11] S. Mekhilef, R. Saidur, and A. Safari, "A review on solar energy use in industries," *Renewable and Sustainable Energy Reviews,* vol. 15, no. 4, pp. 1777-1790, May 2011.

[12] J. K. Kaldellis and D. Zafirakis, "The wind energy (r) evolution: A short review of a long history," *Renewable Energy,* vol. 36, no. 7, pp. 1887-1901, 2011.

[13] Z. Xiudong Tang and Lei, "Vibration energy harvesting from random force and motion excitations," *Smart Materials and Structures,* vol. 21, no. 7, pp. 1887-1901, July 2012.

[14] B. Li, A. J. Laviage, J. H. You, and Y.-J. Kim, "Acoustic Energy Harvesting Using Quarter-Wavelength Straight-Tube Resonator," *Acoustics and Wave Propagation*, vol. 12, pp. 467- 473, Sep. 2012.

[15] C. B. Williams and R. B. Yates, "Analysis of a micro-electric generator for microsystems," *Sensors and Actuators A: Physical,* vol. 52, no. 1, pp. 8-11, April 1996.

[16] R. N. Torah, M. J. Tudor, K. Patel, I. N. Garcia and S. P. Beeby, "Autonomous Low Power Microsystem Powered by Vibration Energy Harvesting," *2007 IEEE Sensors, Atlanta, USA*, pp. 264-267, Oct. 2007.

[17] P. Glynne-Jones, M. Tudor, S. Beeby, and N. White, "An electromagnetic, vibration-powered generator for intelligent sensor systems," *Sensors and Actuators A: Physical*, vol. 110, no. 1-3, pp. 344–349, Feb. 2004.

[18] M. Daniel Hoffmann and Bernd Folkmer and Yiannos, "Fabrication, characterization and modelling of electrostatic micro-generators," *Journal of Micromechanics and Microengineering*, vol. 19, no. 9, pp. 15-18, Aug. 2009.

[19] R. Tashiro, N. Kabei, K. Katayama, E. Tsuboi, and K. Tsuchiya, "Development of an electrostatic generator for a cardiac pacemaker that harnesses the ventricular wall motion," *Journal of Artificial Organs*, vol. 5, no. 4, pp. 239–245, Jan. 2002.

[20] G. K. Ottman, H. F. Hofmann, A. C. Bhatt and G. A. Lesieutre, "Adaptive piezoelectric energy harvesting circuit for wireless remote power supply," in *IEEE Transactions on Power Electronics*, vol. 17, no. 5, pp. 669-676, Sep. 2002.

[21] M. Ferrari, V. Ferrari, M. Guizzetti, D .Marioli, and A. Taroni, "Piezoelectric multifrequency energy converter for power harvesting in autonomous

microsystems," *Sensors and Actuators A: Physical,* vol. 142, no. 1, pp. 329-335, Oct. 2008.

[22] N. Fondevilla, C. Serre, A. Perez-Rodriguez, M. Acero, E. Cabruja, H. Campanella, and J. Esteve, "Electromagnetic harvester device for scavenging ambient mechanical energy with slow, variable, and randomness nature," *2011 International Conference on Power Engineering, Energy and Electrical Drives,* May 2011.

[23] Ö. Zorlu, E. T. Topal and H. Kulah, "A Vibration-Based Electromagnetic Energy Harvester Using Mechanical Frequency Up-Conversion Method," in *IEEE Sensors Journal*, vol. 11, no. 2, pp. 481-488, Feb. 2011.

[24] S. R. Anton and H. A. Sodano, "A review of power harvesting using piezoelectric materials (2003–2006)," *Smart Materials and Structures*, vol. 16, no. 3, pp. 964-1726, May 2007.

[25] J. Bienstman, H. Tilmans, E. Peeters, M. Steyaert, and R. Puers, "An oscillator circuit for electrostatically driven silicon-based one-port resonators," *Sensors and Actuators A: Physical,* vol. 52, no. 1–3, pp. 179-186, March 1996.

[26] H. A. Sodano, D. J. Inman, and G. Park, "A Review of Power Harvesting from Vibration Using Piezoelectric Materials," *The Shock and Vibration Digest,* vol. 36, no. 3, pp. 197-205, 2004.

[27] D. Yoko Ohba and Masahiro Miyauchi and Takaaki Tsurumi and Masaki, "Analysis of Bending Displacement of Lead Zirconate Titanate Thin Film Synthesized by Hydrothermal Method," *Japanese Journal of Applied Physics*, vol. 32, no. 9, pp. 2174-2177, July 1993.

[28] R. G. Ballas, *Piezoelectric multilayer beam bending actuators: Static and dynamic behavior and aspects of sensor integration*. Springer Science, 2007.

[29] "Dynamic behavior of piezoelectric bimorphs," *1993 Proceedings IEEE Ultrasonics Symposium, Baltimore, MD*, vol. 1, pp. 463-465, 1993.

[30] "APC Stripe Actuator," [Online]. Available: https://www.americanpiezo.com/standard-products/stripe-actuators.html. [Accessed: 26-Feb.-2017].

[31] S. Roundy, P. Wright, and J. Rabaey, "A study of low level vibrations as a power source for wireless sensor nodes," *Computer Communications*, vol. 26, no. 11, pp. 1131-1144, Jan. 2003.

[32] H. Li, C. Tian, and Z. D. Deng, "Energy harvesting from low frequency applications using piezoelectric materials," *Applied Physics Reviews,* vol. 1, no. 4, pp.-, Dec. 2014.

[33] H. Sodano, G. Park, D. Leo, and D. J. Inman, "Use of piezoelectric energy harvesting devices for charging batteries," *Proceedings SPIE 5050, Smart Structures and Materials 2003: Smart Sensor Technology and Measurement Systems Conference, San Diago, USA*, pp. 101-108, July 2003.

[34] G. Pfeifer, *Piezoelektrische lineare Stellantriebe*. Techn. Hochsch. Karl-Marx-Stadt, Sekt. Automatisierungstechnik, 1982.

[35] J. Tichý, J. Erhart, E. Kittinger, and J. Prívratská, *Fundamentals of piezoelectric sensorics: mechanical, dielectric, and thermodynamical properties of piezoelectric materials.* Springer Science, 2010.

[36] I. Bork, "Practical tuning of xylophone bars and resonators," *Applied Acoustics,* vol. 46, no. 1, pp. 103-127, Dec. 1995.

[37] S. K. Tang, "On sound transmission loss across a Helmholtz resonator in a low Mach number flow duct," *The Journal of the Acoustical Socity of America,* vol. 127, no. 6, pp. 3519-3525, Jun. 2010.

[38] C. H. Sohn and J. H. Park, "A comparative study on acoustic damping induced by half-wave, quarter-wave, and Helmholtz resonators," *Aerospace Science and Technology,* vol. 15, no. 8, pp. 606-614, Dec. 2011.

[39] M. A. Pillai and E. Deenadayalan, "A review of acoustic energy harvesting," *International Journal of Precision Engineering and Manufacturing,* vol. 15, no. 5, pp. 949-965, May 2014.

[40] C. Chee, L. Tong, and G. Steven, "A mixed model for composite beams with piezoelectric actuators and sensors," *Smart Materials and Structures*, vol. 8, no. 3, pp. 417–432, Jan. 1999.

[41] S. Beheshti-Aval and M. Lezgy-Nazargah, "A Finite Element Model for Composite Beams with Piezoelectric Layers using A Sinus Model," *Journal of Mechanics,* vol. 26, no. 3, pp. 335-344, May 2011.

[42] G. De Abreu, J. Ribeiro, and V. Steffen Jr, "Finite element modeling of a plate with localized piezoelectric sensors and actuators," *Journal of the Brazilian Society of Mechanical Sciences and Engineering*, vol. 26, no. 2, pp. 117-128, Jun. 2004.

[43] R. Zemčík and P. Sadílek, "Modal analysis of beam with piezoelectric sensors a actuators,"*Applied and Computational Mechanics*, vol. 1, no.1, pp. 381-386, Oct. 2007.

[44] B. Adim, T. H. Daouadji, and A. Rabahi, "A simple higher order shear deformation theory for mechanical behavior of laminated composite plates," *International Journal of Advanced Structural Engineering (IJASE),* vol. 8, no. 2, pp. 103-117, May 2016.

[45] D. A. Kross, *A study of stiffness matrices for the analysis of flat plates.* National Aeronautics and Space Administration, 1968.

[46] O. A. Bauchau and J. I. Craig, *Structural Analysis: with Applications to Aerospace Structures*. Springer, pp. 173- 221, 2009.

[47] S. M. Han and H. Benaroya, *Nonlinear and Stochastic Dynamics of Compliant Offshore Structures*. Springer Science & Business Media, 2013.

[48] D. L. Logan, *A First Course in the Finite Element Method*. Cengage Learning, pp. 166-225, 2011.

[49] W. Weaver and J. M. Gere, *Matrix Analysis Framed Structures*. Springer Science, 2012.

[50] M. Avcar, "Free vibration analysis of beams considering different geometric characteristics and boundary conditions," *International Journal of Mechanics and Applications*, vol. 4, no. 3, pp. 94-100, April 2014.

Vita

Maleka Bin Tarsh was born in 1992, in Al-Ain, United Arab Emirates. She received her primary and secondary education in Western Zone, UAE. She received her B.Sc. degree in Electrical and Electronics Engineering from Khalifa University for science and technology in 2014. During her studies, she participated in many competitions locally and internationally.

In February 2015, she joined the Mechatronics Engineering master's program in the American University of Sharjah as a graduate teaching assistant. During her master's study, she was teaching mechanical undergraduate students. Her research interest is in energy and materials.